Nanoscale

PAPER

View Article Online
View Journal | View Issue

Cite this: *Nanoscale*, 2025, **17**, 15731

Nitrogen and sulfur co-doped carbon quantum dot-decorated $Ti_3C_2T_x$-MXenes as electrode materials for high-performance symmetric supercapacitors†

Srija Ghosh,[a] Sumanta Bera,[a] Arijit Kapuria,[a] Anup Debnath,[a,b] Pratyusha Das,[a] Yan-Kuin Su[c] and Shyamal K. Saha *[a,c]

Considering the huge consumption of fossil fuels and cumulative energy demands in the high-tech society, energy storage devices, particularly supercapacitors, play a pivotal role in exploring alternative sources of renewable energy. To focus on potential supercapacitor electrode materials, they should possess essential features such as a massive surface area, good conductivity, and a plentiful number of active sites. Therefore, the integration of a large surface area of two-dimensional (2D) materials with high conductivity with carbon quantum dots (CQDs) containing a large number of active sites is an elegant approach for achieving excellent electrode materials for supercapacitor applications. In the present work, we decorate highly conducting 2D $Ti_3C_2T_x$ MXene sheets with nitrogen (N) and sulfur (S) co-doped CQDs (NS-CQDs) as a source of numerous active sites to explore their potential as electrode materials for supercapacitor applications. We synthesize three samples exhibiting impressive specific capacitances (C_{sp}) of 562.7 F g^{-1}, 725.7 F g^{-1}, and 523.4 F g^{-1}, respectively, at a current density of 1 A g^{-1} with excellent cycling stabilities of 95.5%, 98.3%, and 94.1%, respectively, at a current density of 10 A g^{-1} over 10 000 cycles. The origin of this excellent C_{sp} is the electron clouds near the N- and S-doped atoms which act as active sites. Finally, these unique hybrid composite materials with high C_{sp}, high energy density (170.34 W h kg^{-1} at a power density of 1290.98 W kg^{-1}), and outstanding electrochemical stability show significant promise in the field of storage device applications.

Received 30th November 2024,
Accepted 6th June 2025

DOI: 10.1039/d4nr05037a

rsc.li/nanoscale

1. Introduction

In the modernized world, the growing concerns regarding environmental pollution caused by the consumption of huge amounts of fossil fuels, the increased rate of electrical energy expenditure, and cumulative energy demands have created an imperative urgency to explore and invest in eco-friendly, intermittent, and renewable efficient energy sources as alternatives to fossil fuels to achieve sustainable development for social welfare, economic progression, and environmental protection.[1,2] To confront the existing challenges of accelerated advancements of flexible, portable and wearable electronic devices, incessant research interest has been inclined towards the progression of energy storage systems (such as fuel cells, metal ion batteries, supercapacitors, *etc.*) that are required to meet several specific characteristics such as high energy and power density, long-span cycling stability, high-rate capability, and lower preservation cost.[3] Out of such conventional energy storage devices, supercapacitors (also known as ultracapacitors) have attracted extensive attention in the recent past and are prized for their desirable attributes such as rapid charge–discharge speed, long cycling stability, superior energy density relative to conventional capacitors, greater power density compared to batteries, excellent specific capacity, and green environmental protection.[4] Substantial advancement in the fabrication and composition optimization of one of the prominent components of supercapacitors, *i.e.*, electrodes with commendable intrinsic capacitance, has been concentrated as ongoing startling research interest to ameliorate the efficiency and cycling stability of modern supercapacitor devices.[5] Based on the inherent charge storage mechanisms, supercapacitors are usually divided into two main types: (i) electrochemical

[a]*School of Materials Sciences, Indian Association for the Cultivation of Science, 2A and 2B Raja S. C. Mullick Road, Jadavpur, Kolkata 700032, West Bengal, India. E-mail: cnssks@iacs.res.in, sksaha@gs.ncku.edu.tw*
[b]*Department of Physics, Pachhunga University College, Aizawl, 796001 Mizoram, India*
[c]*Academy of Innovative Semiconductor and Sustainable Manufacturing, National Cheng Kung University, Tainan–701, Taiwan, Republic of China*
† Electronic supplementary information (ESI) available. See DOI: https://doi.org/10.1039/d4nr05037a

double-layer capacitors or EDLCs and (ii) pseudo-capacitors. Extensively used carbon-based electrode materials such as carbon nitrides,[6] carbon nanotubes,[7] carbon nanofibers,[8] *etc.*, basically reputed as EDLC materials, have been restricted in wide-ranging applications because of their lower C_{sp}, low density, and intrinsic energy storage mechanisms.[9] In contrast, conducting polymers and transition metal oxides are thoroughly utilised as pseudo-capacitor materials.[10,11]

Recently, comprehensive research on the fabrication of electrodes with 2D structured materials such as graphene and its composites,[12–14] transition metal dichalcogenides (TMDs),[15] conducting polymers,[16] transition metal oxides,[17] and metal–organic frameworks (MOFs)[18] has garnered immense attention in the realm of electrochemical and energy storage applications. A newly emerging group of transition metal nitrides and carbides (MXenes) has triggered fascinating research attention as potential supercapacitor electrodes because of their unrivaled virtues such as superior electronic conductivity, low work function, enormous surface functional sites, suitable chemical and electrochemical stability, large surface area, surface hydrophilicity, reversible intercalation of positive ions, and impressive mechanical strengths.[19,20] More concretely, MXenes with adequate mechanical flexibility behave as suitable supporting matrices to design hybrid electrodes in advanced energy storage systems.[21] Generally, MXenes with the formula $M_{n+1}X_nT_x$ are synthesized by selective etching out of "A" group layers from bulk MAX phases having the universal formula $M_{n+1}AX_n$ (n = 1, 2, and 3), where "M" depicts early transition metals, "A" denotes group IIIA or IVA elements, "X" denotes either carbon or nitrogen atoms, and "T_x" refers to surface functional groups such as –O, –OH, –F, and –Cl.[22] Among the synthesized diverse MXene materials, $Ti_3C_2T_x$ has been extensively used in supercapacitor applications due to the advantages of MXenes along with its high melting point and Young's modulus, excellent specific surface area, multiple energy storage mechanisms, enriched C_{sp} influenced by redox activity, and exceptional metallic conductivity resulting from an enhanced transition of electrons and ions to electrochemically active sites, which result in good rate performance and better cycling stability.[23,24] The remarkable capacitance in the case of the $Ti_3C_2T_x$ electrode emerges primarily from the following two procedures: (i) formation of an electric double layer caused by adsorption–desorption of ions at the electrolyte–electrode interface and (ii) pseudo-capacitance that is principally attributed to Ti–O bonding and the reversible bonding and de-bonding between –O terminal sites and hydronium ions.[25,26] Nevertheless, the effectiveness of surface terminal groups is interrupted due to the affinity of spontaneous restacking of MXene sheets, driven by intermolecular van der Waals attractive forces between MXene layers. In addition, the effective specific surface area is reduced, the ion transport route is hindered due to the capturing of reaction sites, interlayer spacing is attenuated, and vertical resistance is raised.[27] Consequently, the overall electrochemical performance of MXene-derived supercapacitors suffers a dramatic harm that seriously limits their utility in energy storage applications. To get rid of these knotty problems of self-accumulation, it is our predominant motive to incite the accessibility of surface functional reaction edges by increasing the spacing between $Ti_3C_2T_x$ layers. Researchers have revealed miscellaneous approaches for improving the MXene structure such as sonication in various solvents, self-assembly by electrostatic procedures, incorporation of interlayer spacers with conducting polymers,[28,29] modification with various transition metal oxides,[30,31] and heterostructure composition with manifold 2D materials.[32,33]

On the other hand, CQDs, zero-dimensional quasi-spherical nanoparticles with a crystalline structure, have attracted engrossing research attention in miscellaneous applications such as sensors, optical devices, biomedicines, photocatalysis, electrocatalysis, energy storage devices, *etc.*[34–37] due to their attractive attributes such as the quantum confinement effect, high surface-to-volume ratio, excellent biocompatibility, proper chemical stability, spontaneous aqueous and non-aqueous solubility, tunable optical and electrical properties, facile doping conditions and functionalization, plentiful surface defects,[38,39] and low cost. Along with these engrossing attributes of CQDs, the other appreciable peculiarities are enlarged surface area and abundant edge functional active sites (–OH, –COOH, C–N, *etc.*), making these nanosized materials compatible in supercapacitor applications. These functional groups on the surfaces of CQDs restrain the carbon network and provide harmonization with other operative materials. For example, CQD/metal double hydroxides[40] and CQD/metal oxides (such as MnO_2 and RuO_2)[41,42] have been reported in supercapacitor applications. Still, CQDs face few electrochemical performance complications due to possessing abundant interfaces emerging from internal resistance as well as restacking caused by high surface energy and van der Waals attraction forces. This inconvenience can be overcome proficiently by forming a composite with a conductive matrix or other materials. For example, Jian *et al.* synthesized a CQD/PPy hybrid as a high-performance supercapacitor electrode which has a C_{sp} value of 308 F g^{-1} at a current density of 0.2 mA cm^{-2} with a good capacitance retention of 85.7% over 2000 cycles.[43] Zhao *et al.* designed a unique hybrid-structured electrode material through photo-electrodeposition of polyaniline and CQDs on the surface of carbon fibers. This assembled device exhibits a high C_{sp} value of 738.3 F g^{-1} at a current density of 1 A g^{-1} with a capacitance retention of 78% at a current density of 5 A g^{-1} after 1000 cycles.[44]

Several earlier studies have also focused on fabricating MXene/CQD composites *via* different mechanisms, such as gelation treatment and high-temperature annealing, which may cause partial degradation of MXenes.[45–47] Hetero-atom doping into the CQD network is an elegant approach for enriching the electrochemical activity of pristine CQD host materials and it is reported that hetero-atom doped CQDs exhibit greater specific capacity compared to pristine CQDs. NS-CQDs can preserve exceptional chemical stability and allow achieving excellent charge carrier transport mobility.[48] Indeed, the incorporation of N and S into the CQD network enriches

polar functional groups, thereby improving the surface polarity of CQDs. This effect enhances the interactions between the CQD surface and polar electrolytes. N-containing functionalities, which possess electron-donating properties, further ameliorate electrolyte wettability.[49,50] Moreover, N and S doping creates additional electrochemically active sites at edges, thereby improving pseudocapacitive activity. The simultaneous incorporation of N and S into the CQD lattice leads to the generation of additional trap centers that are responsible for attracting and storing charge carriers and thus the storage capacity is enhanced.[51] Ouyang *et al.* designed an electrode material with S and N co-doped graphene quantum dots with three different doping ratios synthesized using the top-down hydrothermal strategy, and the doped-GQDs show more efficiency than bare GQDs, whereas the co-doped GQDs show the highest C_{sp} of 362.60 F g^{-1} at a scan rate of 5 mV s^{-1} in 2 M KOH. In contrast, GQDs achieve a comparatively lower C_{sp} value of 144.37 F g^{-1} at the same scan rate.[52]

Accordingly, in the present investigation, we have explored a durable and high-performance electrode material for supercapacitor applications by designing NS-CQDs decorated on $Ti_3C_2T_x$ composites. In this interesting 0D/2D (dot/sheet) designed structure, 2D $Ti_3C_2T_x$ acts as a conductive skeleton matrix of this hybrid and NS-CQDs attached onto $Ti_3C_2T_x$ act as a spacer between $Ti_3C_2T_x$ layers, which effectively mitigates the undesirable problem of restacking of $Ti_3C_2T_x$ and is consequently profitable for electrolyte ion adsorption and rapid ion movement activity. Furthermore, the unique surface properties and abundant surface functionalities of NS-CQDs at edges serve as active sites, acting as catalysts in the redox reaction during the procedure of oxidation–reduction. Thus, the coupling of their individual strengths leads to improved pseudo-capacitance, resulting in a comprehensive performance of the supercapacitor. In this work, we have derived three NS-CQD/M composites with three different doping concentrations marked as NS-CQD/M-5, NS-CQD/M-10, and NS-CQD/M-20 using the hydrothermal strategy and their electrochemical performances have been investigated in a symmetric two-electrode device in 1 M H_2SO_4. The composite electrodes of NS-CQD/M-5, NS-CQD/M-10, and NS-CQD/M-20 exhibit impressive C_{sp} values of 562.7 F g^{-1}, 725.7 F g^{-1}, and 523.4 F g^{-1}, respectively, at a current density of 1 A g^{-1} with commendable cycling stabilities of 95.5%, 98.3%, and 94.1%, respectively. Overall, this unique hybrid composite exhibiting a high C_{sp}, high energy and power density, superior rate capacity, and excellent electrochemical stability holds significant promise as an electrode material for supercapacitor applications and its continued modification and progression are anticipated to establish a contribution for advancement in wearable, portable and flexible energy storage technologies.

2. Experimental section

2.1. Chemicals

Titanium aluminium carbide (Ti_3AlC_2) was commercially procured from Nano Research Elements. Hydrochloric acid (HCl, about 37%), citric acid ($C_6H_8O_7$), acetylene black, and ammonia (NH_3) were obtained from Merck chemicals. Lithium fluoride (LiF) and *N*-acetyl L cysteine were purchased from LOBA CHEMIE Pvt Ltd. Nafion, poly-vinylidene fluoride (PVDF), and *N*-methyl-2-pyrrolidinone (NMP) were supplied by Sigma-Aldrich. All the purchased chemicals were of analytical grade and used without any additional purification.

2.2. Preparation of NS-CQDs

NS-CQDs were synthesized *via* a simple one-step hydrothermal treatment. Initially, 100 mg of citric acid as a carbon source was added to 20 ml of deionized (DI) water under continuous stirring at room temperature to prepare a homogeneous solution. After a certain time, 20 mg of *N*-acetyl L cysteine, used the as N and S source, dissolved in 10 ml of DI water was added dropwise to the solution and left under continuous stirring conditions for 30 min. Then ammonia was used to maintain a pH value of 8. The obtained homogeneous solution was transferred into a Teflon-equipped stainless-steel autoclave and kept in a vacuum oven for 8 hours at 120 °C. Then the solution was permitted to cool naturally to room temperature and the transparent solution was filtered through 0.22 μm millipore filter papers to eliminate larger particles. We have prepared the other two NS-CQDs by varying the amount of *N*-acetyl L cysteine, *i.e.*, instead of 20 mg, 5 mg and 10 mg of *N*-acetyl L cysteine dissolved in 10 ml of DI water were added to 20 ml of homogeneous citric acid solution, followed by the above-described process. According to the amount of the source (*N*-acetyl L cysteine) added, the as-prepared NS-CQDs are designated as NS-CQD-5, NS-CQD-10, and NS-CQD-20.

2.3. Synthesis of $Ti_3C_2T_x$

In the first step, 0.8 g of LiF was added to 10 ml of 9 M HCl solution under constant stirring. After 5 min, 0.5 g of the MAX phase (Ti_3AlC_2) powder was added slowly to the above solution to counteract the exothermic reaction and kept under continuous stirring for 24 hours to etch the aluminium (Al) layers from the MAX phase. Next, the obtained solution was washed several times with DI water by centrifugation at a speed of 12 000 rpm for 4 min per cycle until the pH of the acidic supernatant reaches close to neutral. After a few centrifugation cycles, the dark green supernatant was centrifuged again with DI water at a high speed of 3500 rpm for 4 min. Finally, the resulting $Ti_3C_2T_x$ clay was collected and dried under vacuum at temperature 60 °C for 7 h to obtain $Ti_3C_2T_x$ powder.[53]

2.4. Synthesis of the NS-CQD/$Ti_3C_2T_x$ composite

At first, 40 mg of the as-prepared $Ti_3C_2T_x$ was diluted in 20 ml of DI water and sonicated for 3 hours to exfoliate the $Ti_3C_2T_x$ sheets. Then 10 ml of NS-CQDs was added dropwise into the $Ti_3C_2T_x$ dispersion under constant stirring and maintained under these conditions for 1 hour. To avoid over-oxidation of $Ti_3C_2T_x$, Ar gas was injected into the container while stirring. Finally, for the hydrothermal treatment, the mixture was poured into a Teflon-coated sealed autoclave and placed at 180 °C for 6 h. After naturally cooling to room temperature

and filtration, the solution was centrifuged at a speed of 12 000 rpm. Finally, the sample was dried in a vacuum oven and collected as a powder for further experiments. We have prepared three composites and designated as NS-CQD/M-5, NS-CQD/M-10, and NS-CQD/M-20 according to the three different as-synthesized NS-CQDs added during the synthesis of the composite.

For clarity, the complete synthesis strategy for the growth of NS-CQDs on $Ti_3C_2T_x$ sheets to construct the NS-CQD/M composite is schematically illustrated in Fig. 1.

2.5. Materials characterization

To investigate the crystallographic structures of pristine $Ti_3C_2T_x$ and the three composites, powder X-ray diffraction (XRD) measurement was carried out using a RICH SEIFERT-XRD 3000P with a 1.54 Å wavelength monochromatic Cu K_α radiation source with a step size of 0.02° for 2θ. To calculate the interlayer spacing (d-spacing) of the as-prepared samples, we have performed Rietveld refinement with the help of MAUD 2.996 software.[54,55] To explore the surface morphology and microstructure with energy dispersive X-ray (EDX) analysis of the as-synthesized samples, scanning electron microscopy (SEM) images and transmission electron microscopy (TEM) images were obtained using JSM-6360, FE-SEM, JEOL, and TEM instruments, model JEOL-2011, respectively. To understand the elemental composition and chemical bonding states, X-ray photoelectron spectroscopy (XPS) was performed using an OMICRON-0571 system. Contact angle measurements were performed using an Ossila goniometer. Fourier transform infrared (FTIR) spectroscopy measurements were carried out using a NICOLET MAGNA IR 750 spectrometer. The electrochemical performances, *i.e.*, cyclic voltammetry (CV), galvanostatic charge–discharge (GCD), and electrochemical impedance spectroscopy (EIS) analyses of $Ti_3C_2T_x$ and all the composite samples, were performed using a Corr-Test potentiostat/galvanostat electrochemical workstation using symmetric two-electrode cells in 1 M H_2SO_4. The Brunauer–Emmett–Teller (BET) specific surface area, analysed by N_2 adsorption–desorption, and the pore size distribution, determined using the Barrett–Joyner–Halenda (BJH) method, were characterized using Autosorb iQ Station 1.

2.6. Device fabrication for electrochemical measurements

For fabrication of a working electrode, 85 wt% of active material, 5 wt% of acetylene black, and 10 wt% of PVDF solution in NMP solvent and Nafion were mixed thoroughly to form a homogeneous slurry and it was coated on two coin cells of nickel. Here, acetylene black and Nafion were used to enhance the overall conductivity and PVDF was utilised as a binder. The electrode pieces were dried at 50 °C under vacuum conditions for 6 h. The painted sides were sandwiched with a filter paper wetted with 1 M H_2SO_4 electrolyte, acting as separator, and mass loading per unit active area was 2 mg cm^{-2}.

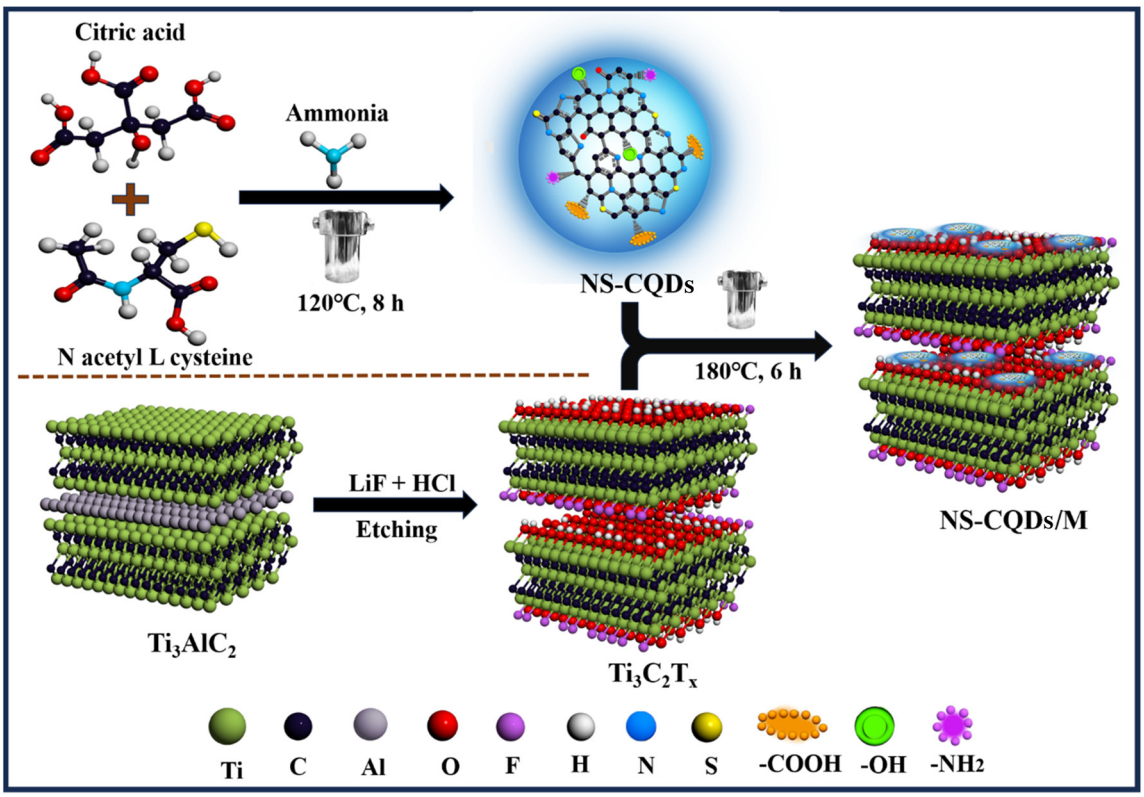

Fig. 1 Schematic illustration of the synthesis procedures of NS-CQDs, $Ti_3C_2T_x$ from Ti_3AlC_2, and the NS-CQD/M composite.

CV analyses were conducted in the potential range between −0.65 V and +0.65 V at various scan rates from 10 mV s^{-1} to 50 mV s^{-1}. GCD experiments were conducted at several current densities of 1, 2, 3, 4, 5, 10, 15, and 20 A g^{-1} within a voltage range of −0.65 V to +0.65 V. EIS spectra were recorded over the frequency range from 0.01 Hz to 100 kHz.

The value of gravimetric C_{sp} was determined from CV curves using the following formula:[56]

$$C_{sp}\left(\mathrm{F\,g^{-1}}\right) = \frac{\int_{V_i}^{V_f} I(V)\mathrm{d}V}{Mv(V_f - V_i)} \quad (1)$$

where M represents the loaded mass (g) of the active material, v is the scan rate (mV s^{-1}), V_f and V_i are the upper and lower limits of the potential window, and $\int_{V_i}^{V_f} I(V)\mathrm{d}V$ refers to the overall integrated area under CV curve.

The C_{sp} value was evaluated from the GCD curves according to the formula:[57]

$$C_{sp}\left(\mathrm{F\,g^{-1}}\right) = \frac{2I\Delta t}{M\Delta V} \quad (2)$$

where I, Δt, M, and ΔV denote the discharging current (A), discharging time (s), loaded mass (g) of the active electrode material, and cell potential (V), respectively.

The energy density (E) and power density (P) were obtained using the following equations:[58]

$$E(\mathrm{W\,h\,kg^{-1}}) = \frac{C \times (\Delta V^2)}{2 \times 3.6} \quad (3)$$

$$P(\mathrm{W\,kg^{-1}}) = \frac{E \times 3600}{\Delta t} \quad (4)$$

where C, Δt, and ΔV are the C_{sp} value from eqn (2), discharging time (s), and potential window (V), respectively.

3. Results and discussion

3.1. Surface morphology and elemental analysis

FE-SEM images of pristine $Ti_3C_2T_x$ and the NS-CQD/M-5, NS-CQD/M-10, and NS-CQD/M-20 composites are shown in Fig. 2(a–d) to investigate the surface morphology. Fig. 2(a) illustrates that pristine $Ti_3C_2T_x$ consists of a typical laminar structure, *i.e.*, stacked 2D sheets. According to Fig. 2(b–d), the composites preserve the original topography, *i.e.*, a layer-by-layer configuration. The EDX spectra of $Ti_3C_2T_x$ and the composites, presented in Fig. S1(a–d),† illustrate a homogeneous distribution of Ti, C, O, F, N, and S elements, confirming the

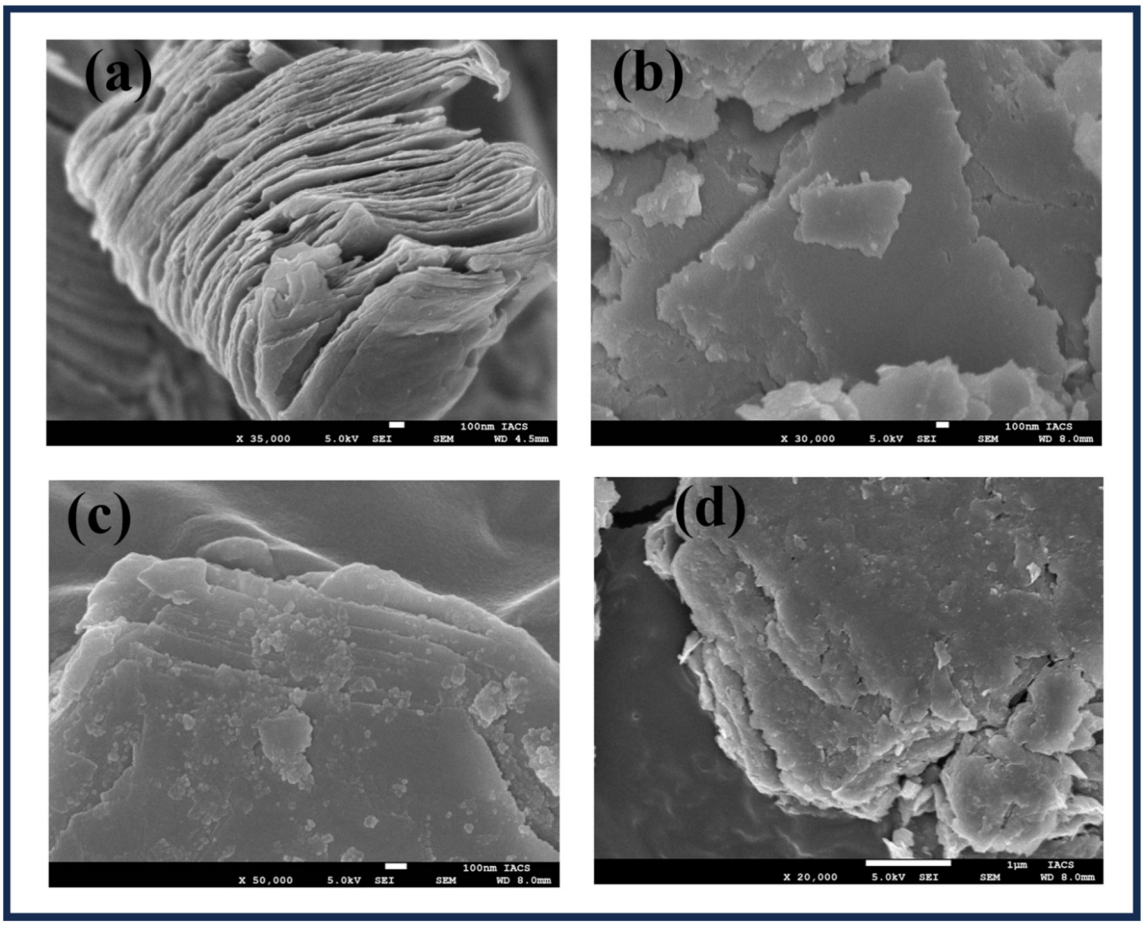

Fig. 2 SEM images of (a) $Ti_3C_2T_x$, (b) NS-CQD/M-5, (c) NS-CQD/M-10, and (d) NS-CQD/M-20.

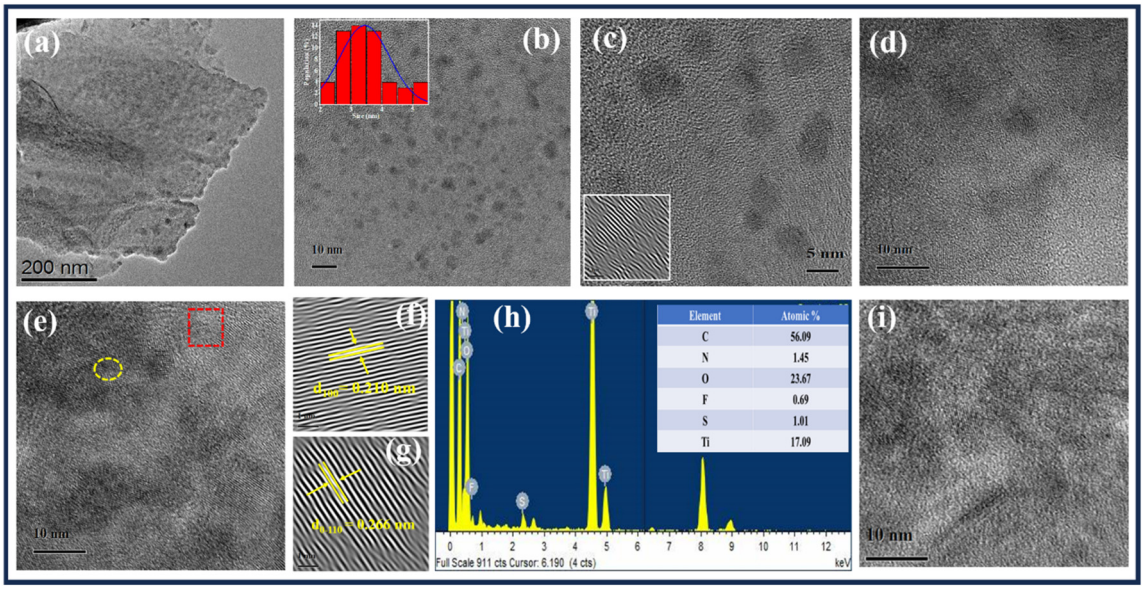

Fig. 3 TEM images of (a) pristine $Ti_3C_2T_x$ and (b) bare NSCQD-10 (inset: particle size distribution); high-resolution TEM images of (c) bare NSCQD-10 (inset: IFFT fringe pattern), (d) NS-CQD/M-5 and (e) NS-CQD/M-10; (f) and (g) IFFT fringe pattern of the marked portion, (h) corresponding EDX spectrum with the atomic percentage of NS-CQD/M-10, and (i) high-resolution TEM image of NS-CQD/M-20.

successful incorporation of NS-CQDs within the $Ti_3C_2T_x$ matrix.

To explore the microstructures of the samples in detail, TEM of bare $Ti_3C_2T_x$ along with the as-synthesized bare NS-CQD-10 and the three composites were conducted and the images are shown in Fig. 3. Fig. 3(a) represents the 2D layer configuration of pristine $Ti_3C_2T_x$. From Fig. 3(b and c), the high-resolution TEM (HR-TEM) images of bare NS-CQD-10, it is clearly observed that NS-CQDs occupy a homogeneous dispersion without agglomeration with a particle size distribution in the range of 2–6 nm and the statistical histogram representing the mean size of NS-CQDs is displayed in the inset of Fig. 3(b). The average particle size of NS-CQDs is around 3.46 ± 0.09 nm. As demonstrated in the inset of Fig. 3(c), it is perceived that the lattice fringes of distinct NS-CQD-10 ensure a proper crystallinity with a lattice spacing of 0.211 nm, which is attributed to the (100) lattice orientation of NS-CQDs.[59] Fig. 3(d) and Fig. S2(a)† display the HR-TEM image and the corresponding EDX spectrum of the NS-CQD/M-5 composite, respectively. Fig. 3(e) exhibits an HR-TEM image of the NS-CQD/M-10 composite in which two different types of fringe patterns are located. The yellow-coloured circular specified section and the red-coloured rectangular marked section correspond to NSCQDs and Ti_3C_2-MXene respectively. Fig. 3(f) and (g) illustrate the fringe patterns obtained from the inverse fast Fourier transform (IFFT) procedure with *d*-spacing values 0.210 nm and 0.266 nm (ref. 60) correlated to the (100) plane orientation of NS-CQDs and the (0−110) lattice orientation of $Ti_3C_2T_x$, respectively. The EDX spectrum of the hybrid NS-CQD/M-10 is shown in Fig. 3(h). The TEM image of NS-CQD/M-20 and the corresponding EDX spectrum are displayed in Fig. 3(i) and Fig. S2(b),† respectively. It is salient that the amount of N and S increases from the NS-CQD/M-5 composite to the NS-CQD/M-20 composite sequentially, corroborating the growth of NS-CQDs on the $Ti_3C_2T_x$ layers. The elemental mappings of the NS-CQD/M-10 composite (Fig. S3†) show that N and S heteroatoms are uniformly distributed throughout the mapped area, which further ensures the successful introduction of NS-CQDs within the Ti_3C_2-MXene supporting matrix. This result is due to the surface functional groups of both $Ti_3C_2T_x$ and NS-CQDs through forming covalent C–O–Ti bonding at the hetero-connection of the NS-CQD/M hybrid.

3.2. Analysis of XRD patterns

The crystal structures of all the as-prepared composites along with pristine $Ti_3C_2T_x$ and the precursor Ti_3AlC_2 (MAX phase) were examined using powder XRD. As shown in Fig. S4,† one of the most prominent diffraction peaks of the MAX phase observed at a 2θ value of 38.75°, indicating the (104) plane evolved by the Ti–Al bond, completely disappears in the etched $Ti_3C_2T_x$ phase because of etching out of Al layers and exfoliation.[61] Furthermore, a diffraction peak of the MAX phase at a 2θ value of 9.52°, indicating the (002) plane correlated to an interlayer spacing (*d*-value) of 9.27 Å, is significantly left-shifted in $Ti_3C_2T_x$ at a 2θ value of 7.00° corresponding to the *d*-value of 12.60 Å, which confirms the expansion of inter-layer spacing due to etching treatment and link-up of surface functional groups (–OH, –O, –F, *etc.*) on the $Ti_3C_2T_x$ surface.[62] XRD patterns of the three studied composite materials in comparison with that of bare $Ti_3C_2T_x$ are displayed in Fig. 4(a). The peaks for the (002) planes of three composite samples, *i.e.*, NS-CQD/M-5, NS-CQD/M-10, and NS-CQD/M-20, appear at the 2θ positions of 6.87°, 6.85°, and 6.82°, corresponding to the *d*-values of 12.85, 12.91, and 12.95 Å, respectively. In the three

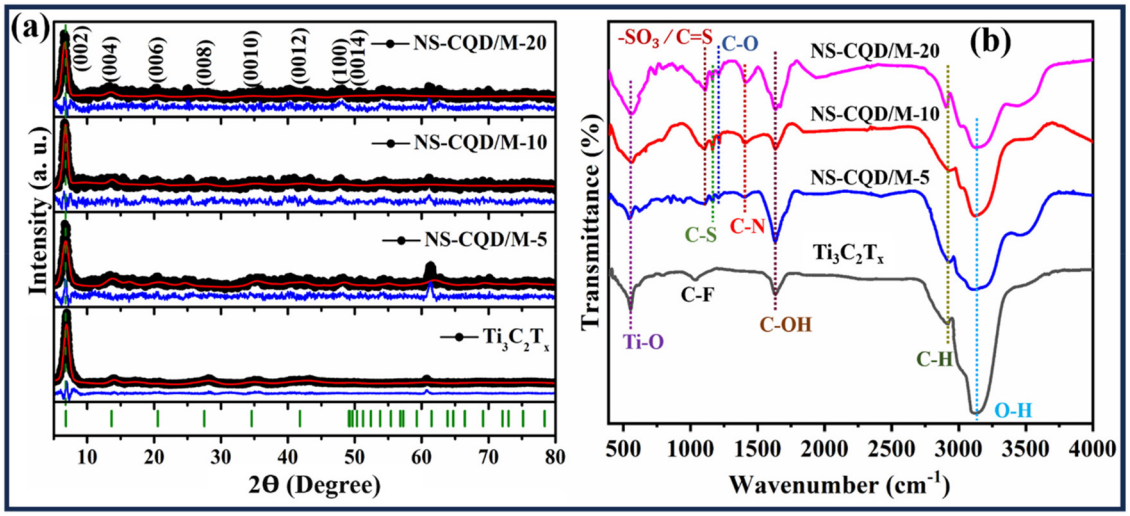

Fig. 4 (a) X-ray diffraction patterns and (b) FTIR spectra of pristine $Ti_3C_2T_x$ along with all the three as-prepared composites.

composite samples, a slight left-shift of the (002) plane with respect to its position in the bare $Ti_3C_2T_x$ sample is observed, evidencing that the introduction of NS-CQDs onto the $Ti_3C_2T_x$ surface is responsible to the enlargement of interlayer spacing and the detract restacking of 2D $Ti_3C_2T_x$ MXene sheets.

3.3. Analysis of FTIR spectra

To investigate the surface functional groups of the three as-prepared composites and those of pristine $Ti_3C_2T_x$, FTIR spectroscopy was performed within the wavenumber ranging from 400 to 4000 cm^{-1} and the spectra of all the as-synthesized samples are shown in Fig. 4(b). The FTIR spectrum of bare $Ti_3C_2T_x$ shows a widespread absorption peak at 3130 cm^{-1} corresponding to the asymmetric stretching vibration of O–H. Simultaneously, the peaks at 555 cm^{-1}, 1036 cm^{-1}, 1633 cm^{-1}, and 2920 cm^{-1} are attributed to the Ti–O deformation vibration, C–F stretching vibration, C–OH bending vibration, and C–H symmetric stretching vibration, respectively.[63,64] Moreover, all three as-prepared hybrids show additional characteristic peaks along with the previously discussed absorption peaks. In particular, the absorption peak at 1405 cm^{-1} corresponds to the stretching vibration of C–N; the peak at 1107 cm^{-1} represents the $-SO_3$ or C═S group; the peaks at 1166 cm^{-1} is ascribed to C–S stretching frequency; the peak at 1209 cm^{-1} shows the existence of the C–O group.[65,66] Hence, all the absorption peaks that emerged in the as-synthesized composites assure the attachment of NS-CQDs to the $Ti_3C_2T_x$ matrix. The relative intensities of the peaks for the C–N and C–S stretching vibrations increase from the NS-CQD/M-5 composite to the NS-CQD/M-20 composite, signifying the increase of the doping concentration of N and S in the CQD network over $Ti_3C_2T_x$ sheets.

3.4. Analysis of XPS spectra

The chemical bonding and surface elemental composition of the all as-prepared samples were thoroughly analysed using X-ray photoelectron spectroscopy (XPS). The full-range XPS spectra of pristine $Ti_3C_2T_x$ and the NS-CQD/M-5, NS-CQD/M-10, and NS-CQD/M-20 composites, as shown in Fig. S5(a), S6(a),† Fig. 5(a), and Fig. S7(a),† respectively, confirm the presence of the characteristic peaks (Ti 2p, Ti 2s, C 1s, O 1s, O 2s, and F 1s) of the compositional elements. All the XPS spectra were analysed relative to the shift of the standard C 1s peak.[67,68] The high-resolution XPS peaks corresponding to the compositional elements of pristine $Ti_3C_2T_x$ are shown in Fig. S5(b–d).† The deconvoluted C 1s spectrum (Fig. S5(b)†) shows peaks at 281.83 eV (C–Ti), 284.78 eV (C═C/C–C), and 286.07 eV (C–O).[69,70] The Ti 2p spectrum (Fig. S5(c)†) was deconvoluted into four component peaks (such as Ti–C, Ti(II), Ti(III), and Ti–O), each splits into two doublets $2p_{3/2}$ and $2p_{1/2}$, in addition to one Ti–F bond. The Ti $2p_{3/2}$ peaks appear at 455.30 eV (Ti–C), 456.44 eV (Ti(II)), 457.50 eV (Ti(III)), and 459.13 eV (Ti–O), while the Ti $2p_{1/2}$ peaks appear at 460.90 eV (Ti–C), 461.90 eV (Ti(II)), 463.00 eV (Ti(III)), and 464.80 eV (Ti–O).[70] The component peak at 459.60 eV corresponds to the Ti–F bond, which confirms the presence of the F functional group attached to the $Ti_3C_2T_x$ sheets. Fig. S5(d)† shows the O 1s spectrum, deconvoluted into sub-peaks at 529.47 eV (Ti–O), 530.33 eV (C–Ti–O_x), 532.26 eV (C–Ti–$(OH)_x$), and 533.82 eV (C–O/H_2O).[71]

The high-resolution XPS spectra corresponding to the compositional elements (C 1s, Ti 2p, O 1s, N 1s, and S 2p) of the NS-CQD/M-10 composite are shown in Fig. 5(b)–(f). The deconvoluted C 1s spectrum (Fig. 5(b)) shows peaks at 281.81 eV (C–Ti), 284.71 eV (C═C/C–C), 285.26 eV (C–S), 286.25 eV (C–N), 286.83 eV (C–O–Ti), and 288.79 eV (C═N/O═C–O).[72,73] Notably, the presence of the C–O–Ti peak indicates a strong covalent bonding, which enhances the attachment of NS-CQDs to $Ti_3C_2T_x$, contributing to the composite's architecture. The Ti 2p spectrum (Fig. 5(c)) was deconvoluted into four component bonds (such as Ti–C, Ti(II), Ti(III), and Ti–O), each splits into two doublets $2p_{3/2}$ and $2p_{1/2}$. The Ti $2p_{3/2}$ peaks

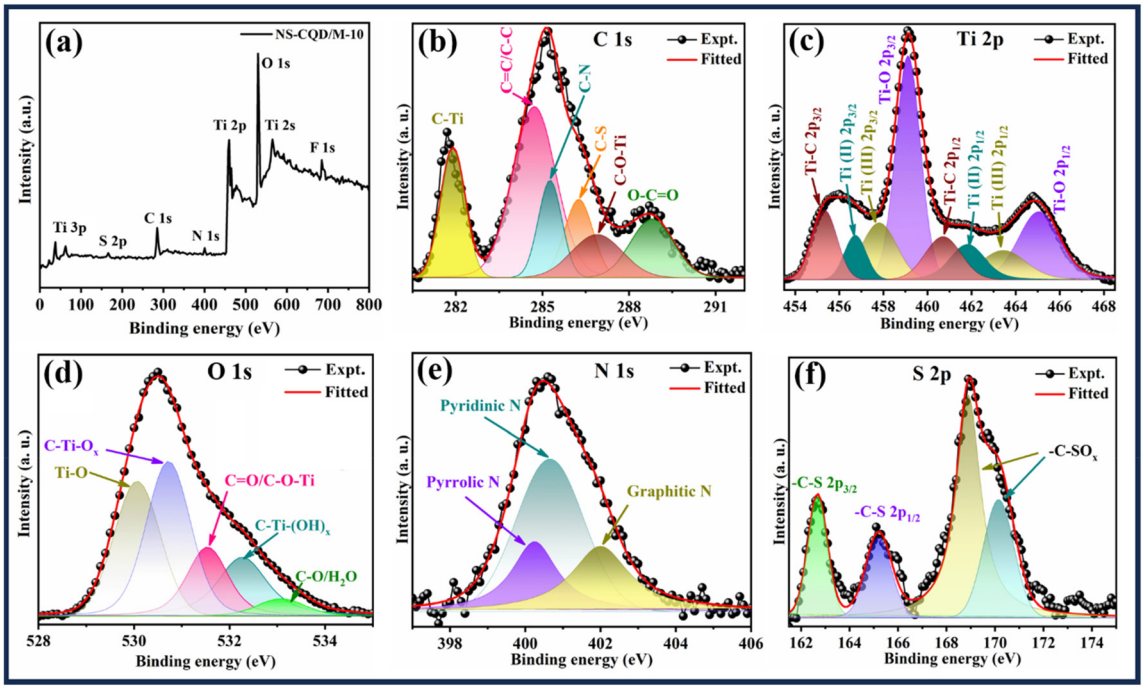

Fig. 5 XPS spectra of NS-CQD/M-10: (a) full range spectrum and deconvoluted high-resolution spectra of (b) C 1s, (c) Ti 2p, (d) O 1s, (e) N 1s, and (f) S 2p.

appear at 455.33 eV (Ti–C), 456.32 eV (Ti(II)), 457.41 eV (Ti(III)), and 459.11 eV (Ti–O), while the Ti $2p_{1/2}$ peaks appear at 460.31 eV (Ti–C), 461.81 eV (Ti(II)), 463.43 eV (Ti(III)), and 465.05 eV (Ti–O). Fig. 5(d) shows the O 1s spectrum deconvoluted into sub-peaks at 530.06 eV (Ti–O), 530.72 eV (C–Ti–O_x), 531.54 eV (C═O/C–O–Ti), 532.26 eV (C–Ti–$(OH)_x$), and 533.08 eV (C–O/H_2O).[71,73] These peaks indicate the linkage of NS-CQDs with the terminal functional groups of the $Ti_3C_2T_x$ matrix. Pristine $Ti_3C_2T_x$ sheets typically stack together, inhibiting ion transport and forming Ti–O bonds to enhance pseudo-capacitance. The attachment of NS-CQDs *via* C–O–Ti covalent bonds at the heterojunction increases interlayer spacing, a phenomenon confirmed by XRD analysis, which shows a left shift in the (002) plane for the NS-CQD/M hybrid. The high-resolution N 1s spectrum (Fig. 5(e)) shows sub-peaks at 400.24 eV, 400.65 eV, and 401.99 eV, corresponding to pyridinic N, pyrrolic N, and graphitic N, respectively.[74] These findings confirm the N doping into CQDs in the composite. Graphitic N enhances charge transport, while pyrrolic N and pyridinic N improve redox behaviour. Additionally, these N species donate π electrons to the CQD network, increasing the electrical conductivity and enhancing the pseudocapacitive performance.[74] Lastly, the S 2p spectrum (Fig. 5(f)) was deconvoluted into sub-peaks at 162.67 eV (C–S $2p_{3/2}$), 165.19 eV (C–S $2p_{1/2}$), 168.89 eV (C-SO_x), and 170.14 eV (C–SO_x), manifesting S-doping into CQDs in the composite.[48] In addition, the XPS spectra of the other two composites, NS-CQD/M-5 and NS-CQD/M-20, shown illustrated in Fig. S6 and S7,† respectively. The peak positions corresponding to the characteristic bonds in the NS-CQD/M-5 and NS-CQD/M-20 samples are consistent with those of the NS-CQD/M-10 sample. This indicates an appropriate interaction between the NS-CQDs and the $Ti_3C_2T_x$ MXene in all three composite samples.

3.5. Electrochemical study

To investigate the intrinsic electrochemical behaviour of the as-synthesized NS-CQD/M hybrids in comparison with that of pristine $Ti_3C_2T_x$ as supercapacitor electrodes intuitively, CV and GCD studies were carried out with assembling a two-electrode symmetric device structure (NS-CQD/M//NS-CQD/M) in an 1 M H_2SO_4 electrolyte solution. All of the electrode materials respond to a suitable potential window of −0.65 to +0.65 V. From the CV curves, the C_{sp} values were calculated by evaluating the computational value of the area under the CV curves following eqn (1). The CV profiles of bare $Ti_3C_2T_x$ and the NS-CQD/M-5 to NS-CQD/M-20 composites at different scan rates ranging from 10 to 50 mV s^{-1} were recorded and are shown in Fig. 6(a–d), respectively, and the C_{sp} values evaluated from the CV profiles at various scan rates are presented in Table S1.† The C_{sp} value for bare $Ti_3C_2T_x$ (shown in Fig. 6(a)) is obtained as 243.8 F g^{-1} at a scan rate of 10 mV s^{-1} and it exhibits the lowest C_{sp} value among the as-synthesized $Ti_3C_2T_x$ composites. The gravimetric C_{sp} value tested for NS-CQD/M-5 (shown in Fig. 6(b)) is found to be 573.0 F g^{-1}, which is a comparatively higher value than bare $Ti_3C_2T_x$ at the same scan rate, whereas the NS-CQD/M-10 composite (shown in Fig. 6(c)), with more doping concentrations of N and S heteroatoms than the former, shows a C_{sp} value of 709.3 F g^{-1} which is the

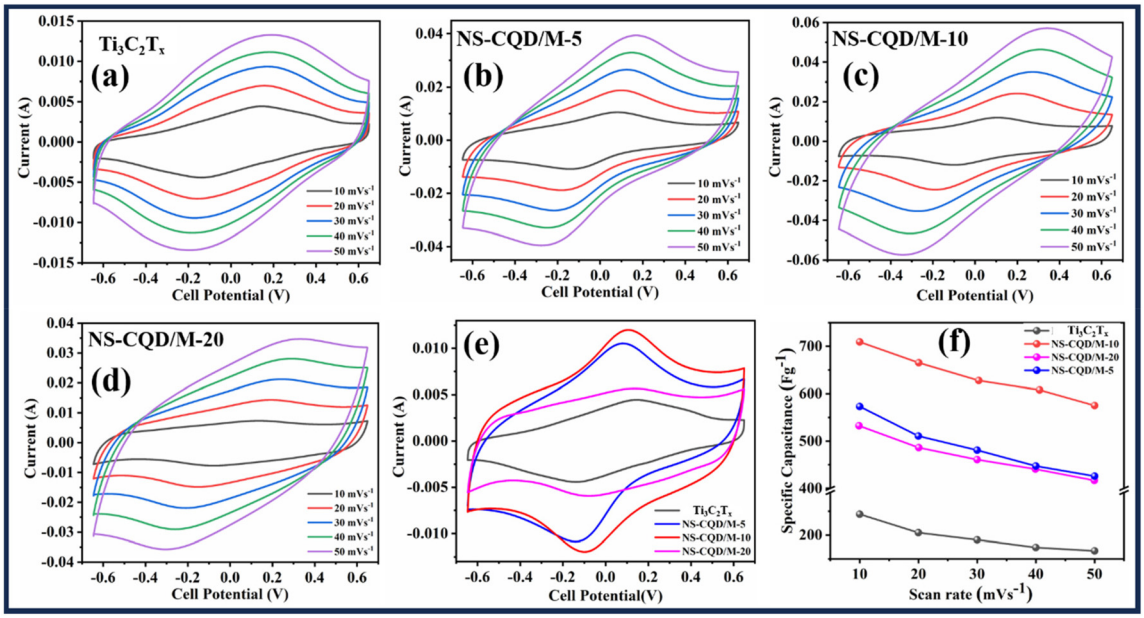

Fig. 6 CV curves of (a) bare $Ti_3C_2T_x$, (b) NS-CQD/M-5, (c) NS-CQD/M-10, (d) NS-CQD/M-20, (e) all the composites in comparison with pristine $Ti_3C_2T_x$ at a fixed scan rate of 10 mV s^{-1}, and (f) comparison of specific capacitances of all the composites at varying scan rates.

highest value of C_{sp}. In contrast, the gravimetric C_{sp} value for the composite of utmost dopant concentration of N and S, *i.e.*, NS-CQD/M-20 (shown in Fig. 6(d)), is obtained as 532.4 F g^{-1}, which is smaller than both of NS-CQD/M-5 and NS-CQD/M-10 but higher than that of bare $Ti_3C_2T_x$. The CV curves of bare $Ti_3C_2T_x$ along with the as-synthesized composites at a static scan rate of 10 mV s^{-1} are shown in Fig. 6(e) and it is apparent that the most proficient hybrid NS-CQD/M-10 maintains the largest CV integrated area compared to bare $Ti_3C_2T_x$ and the other two as-prepared hybrids. It can be proposed that the shapes of CV profiles remain undistorted at higher scan rates, confirming the suitable rate capability and interfacial kinetics of the as-obtained samples. Notably, the electrochemical performance of the as-synthesized materials decreases with increasing scan rates because of the obstruction of diffusion of charged ions and absorption of ions to the electrode surface.

The CV curves of bare $Ti_3C_2T_x$ consist of a pair of noticeable oxidation–reduction peaks that confirm a faradaic charge storage mechanism. In fact, negatively charged 2D $Ti_3C_2T_x$ possessing negative functional groups (*i.e.* –F, –OH, –O, *etc.*) exhibits an electrochemical double layer charge storage mechanism at the interface because of the electrostatic attraction of opposite charges. Collaterally, negatively charged $Ti_3C_2T_x$ shows pseudo-capacitance due to the bonding of hydronium ions (H^+) from the H_2SO_4 electrolyte and the –O terminal interfacial functional groups of $Ti_3C_2T_x$. In consequence of debonding, the oxidation valence state of Ti is between +3 and +4, and the faradaic process which contributes to the redox peaks of the CV curves of $Ti_3C_2T_x$ can be followed as:[60]

$$Ti_3C_2O_x + \delta e^- + \delta H^+ = Ti_3C_2O_{x-\delta}(OH) \quad (5)$$

$$Ti_3C_2O_x(OH)_yF_z + \delta e^- + \delta H^+ \rightarrow Ti_3C_2O_{x-\delta}(OH)_{y+\delta}F_z \quad (6)$$

It is noteworthy that CQDs, *i.e.*, carbonaceous electrodes, exhibit a capacitor-like quasi-rectangular CV profile by undergoing an electrical double-layer charge storage (EDLC) mechanism. However, the deviation from the rectangular shape and a pair of magnificent redox peaks owing to the increased current value in all the CV curves of the as-prepared samples indicate the pseudocapacitive behaviour of the charge storage mechanism. Thanks to $Ti_3C_2T_x$ as a potent conductive supporting system to this hybrid, it not only supplies the adequate surface area but also encourages long-range electronic conductivity by reducing internal resistance and assures proficient electron transport throughout the electrode material. N and S co-doping in the CQD network enhances electrolyte wettability, as evidenced by contact angle measurements shown in Fig. S8.† Actually, N and S co-doping into a low-dimensional CQD network plays a crucial role in acting as a spacer between the lamellar structure of pristine $Ti_3C_2T_x$ sheets and thus NS-CQDs provide a stable interlayer framework that enhances the effective surface area through exfoliation, preventing face-to-face self-restacking between $Ti_3C_2T_x$ sheets. Consequently, the interlayer spacing between $Ti_3C_2T_x$ sheets is expanded, which is advantageous for ion adsorption, and facilitates the transport of charged ions from the electrolyte into the interlayers of $Ti_3C_2T_x$ sheets. This also promotes the evolution and exposure of additional redox-active sites at the heterojunction of the composite. It is observed that the oxidation–reduction peaks are prominent in the case of $Ti_3C_2T_x$ hybrids compared to pristine $Ti_3C_2T_x$ with higher current values, resulting in an enhancement of the CV integrated area because of the reversible redox reaction of N and S heteroatoms contributes to

pseudo-capacitance. Indeed, CQDs with a low dimensional configuration provide a large-scale specific surface area to expound enormous redox active sites. Additionally, CQDs provide additional Ti–O functional sites with the Ti_3C_2-MXene matrix and the N,O-containing functional sites, *i.e.*, the hydrophilic functional groups on the surface of NS-CQDs increase hydrophilicity on the surface of composite electrodes towards the solvent, which diminishes the mass transfer resistance contributing an overall improvement of the pseudo-capacitive performance. Furthermore, the N- and S-doped states within CQDs contribute to additional electrochemically active sites at edges through constructing plenty of defects and S-doped states can rectify the localized electronic state and the Fermi level as well as promote the mobility of carrier transport,[75] emerging an enhancement of pseudo-capacitive efficiency. As a result of N doping, not only conjugation occurs between the C lattice π system and the lone pair electrons of N but also a compatible polarization is formed due to considerable difference in the electronegativity of N atoms (3.05) and C atoms (2.55). In the case of S doping, a discrepancy arises because of the inhomogeneous spin density distribution of the outermost orbitals of C and S as well as polarization is raised due to a minute difference in the electronegativity of C atoms and S atoms (2.58).[75] Accordingly, this distinctive co-doping modification sustains excellent chemical stability and stimulates good carrier transport mobility. Another argument regarding improved pseudocapacitive behaviour is due to the reverse redox reaction through the exchange of positive ions between the acidic electrolyte solution and the electrochemically reactive sites of NS-CQDs. Besides, N- and S-doped states act as additional trap states that ameliorate charge storage capacity through storing charge carriers[51] as well as the variation of electronic charge density leads to ion adsorption that is responsible for the betterment of double-layer capacitance.[76] In this fashion, the synergistic effect of the introduction of low dimensional CQDs within the $Ti_3C_2T_x$ matrix and N and S co-doping modification assist in heightened pseudocapacitive performance. It is also to be noted that the NS-CQD/M-20 sample, *i.e.*, the composite of $Ti_3C_2T_x$ with the highest doping concentration of N and S in CQDs, exhibits a lower C_{sp} compared to the other two doped hybrids because of the fact that for too many dopants, the overall conductivity of the $Ti_3C_2T_x$ backbone for charge transport decreases and higher concentration of N and S evolve additional oxygen (O) vacancies compensating the effectiveness of impurity atoms, thereby resulting in reduced capacitive performance.

Besides that, the type of capacitance, *i.e.*, the charge storage mechanism of the as-synthesized materials, was analysed by following the power law $i_p = av^b$, where i_p denotes the peak current associated with the scan rate v from the CV curve and a and b are proportionality constants. The scheme of capacitance is determined by the b value which is estimated from the slope of the linear plot of $\log i_p$ *vs.* $\log v$ that is shown in Fig. 8 (a and b). b = 0.5 explains the faradaic charge transport, *i.e.*, the diffusion-controlled mechanism of charge storage, whereas b = 1 explains the non-faradaic process, *i.e.*, the surface-controlled reaction.[60] The values of b are 0.68, 0.81, 0.89, and 0.92 in the case of anodic peak current, whereas the values of b are 0.69, 0.80, 0.88, and 0.92 in the case of cathodic peak current for bare $Ti_3C_2T_x$, NS-CQD/M-5, NS-CQD/M-10, and NS-CQD/M-20, respectively. This corroborates that the as-synthesized composite materials confirm domination of the surface-controlled charge storage mechanism rather than the diffusion-controlled mechanism.

To further investigate the precise contributions of capacitive-controlled and diffusion-controlled capacities, the CV curves of all as-synthesized samples were explored by following Dunn's equation:

$$i(V) = k_1 v + k_2 v^{\frac{1}{2}} \quad (7)$$

where $i(V)$ is the CV current at voltage V, while k_1 and k_2 are constants, and v is the scan rate. The terms k_1v and $k_2v^{\frac{1}{2}}$ are the capacitive-controlled and diffusion-controlled contributions, respectively.[60] The values of k_1 and k_2 can be easily obtained from the slope and the Y-axis intercept of the plotted graph $\frac{i(V)}{v^{\frac{1}{2}}}$ *vs.* $v^{\frac{1}{2}}$ (Fig. 8(c)). The percentages of capacitive-controlled and diffusion-controlled contributions for bare $Ti_3C_2T_x$, NS-CQD/M-5, NS-CQD/M-10, and NS-CQD/M-20 are presented in Fig. 8(d–g).

Moreover, another significant parameter, *i.e.*, the percentage retention of the as-synthesized materials was calculated. The best-performing sample NS-CQD/M-10 exhibits remarkable capacity retention. At a scan rate of 50 mV s^{-1}, this material has retained 81.09% of its C_{sp} value compared to the C_{sp} value at a scan rate of 10 mV s^{-1}. However, pristine $Ti_3C_2T_x$, NS-CQD/M-5, and NS-CQD/M-20 have retained 68.45%, 74.29%, and 78.25%, respectively, of their capacitance values at a scan rate of 50 mV s^{-1}. Fig. 6(f) shows a graphical histogram of the C_{sp} values of the samples with different scan rates.

The GCD curves of bare $Ti_3C_2T_x$ and the three composites NS-CQD/M-5, NS-CQD/M-10, and NS-CQD/M-20 were recorded and are displayed in Fig. 7(a–d), respectively, within the same potential window of −0.65 V to +0.65 V at discrete current densities of 1, 2, 3, 4, 5, 10, 15, and 20 A g^{-1}. The gravimetric C_{sp} value can be estimated from the discharging time of GCD curves following eqn (2). In addition, all the C_{sp} values, evaluated from the GCD curves of the investigated samples at several current densities, are presented in Table S2.† Fig. 7(e) depicts the comparative GCD curves of pristine $Ti_3C_2T_x$ along with its three hybrids at a static current density of 1 A g^{-1}. Here, we observed the non-linear, triangular, and symmetric forms of GCD curves, indicating the pseudocapacitive charge storage mechanism of the studied materials.[23] Besides, there is no distinct IR drop in the GCD curves which also ensures less internal resistance and proper electrochemical kinetics as well. The discharging times of the three $Ti_3C_2T_x$ hybrids are greater than that of bare $Ti_3C_2T_x$, and NS-CQD/M-10 in comparison with the other two composites has a strikingly higher discharging time than $Ti_3C_2T_x$ as expected from previous ana-

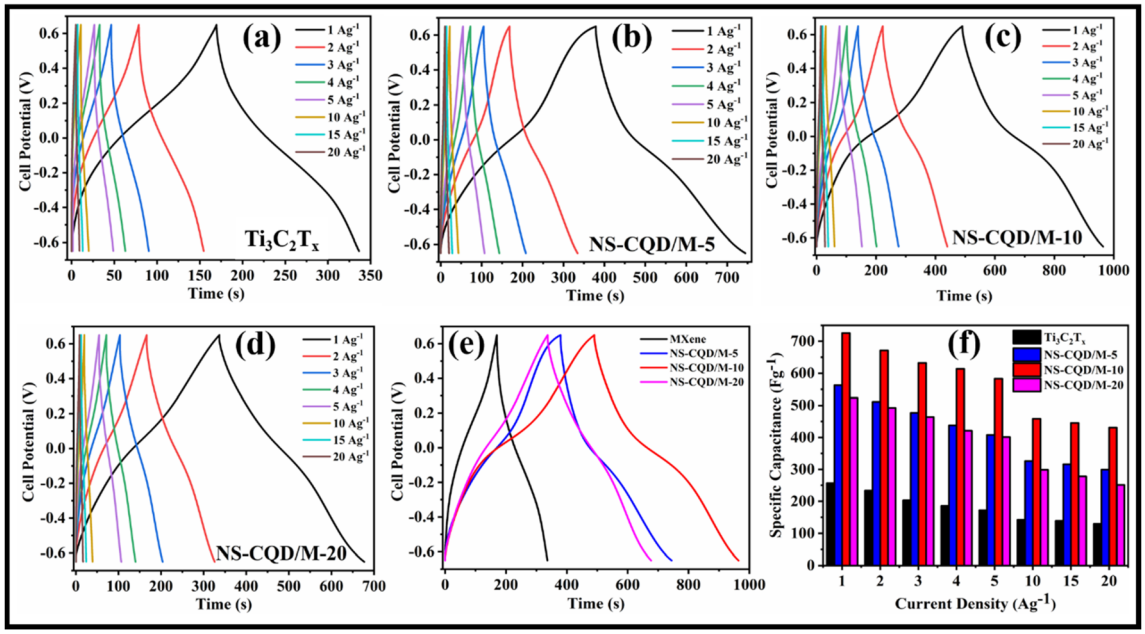

Fig. 7 GCD curves of (a) $Ti_3C_2T_x$, (b) NS-CQD/M-5, (c) NS-CQD/M-10, (d) NS-CQD/M-20, (e) all the composites in comparison with pristine $Ti_3C_2T_x$ at a fixed current density of 1 A g^{-1}, and (f) comparison of specific capacitances of all the composites at varying current densities.

lysis. It is obvious that among the composites, NS-CQD/M-10 shows the maximum gravimetric C_{sp} value of 725.7 F g^{-1}, whereas the calculated C_{sp} values for NS-CQD/M-5 and NS-CQD/M-20 are 562.7 F g^{-1} and 523.4 F g^{-1}, respectively, at a current density of 1 A g^{-1}. Bare $Ti_3C_2T_x$ exhibits a C_{sp} value of 256.8 F g^{-1} at the same current density, which reflects as the lowest among the C_{sp} values of the other three composites. A histogram illustrating the C_{sp} values of all the studied materials at current densities of 1, 2, 3, 4, 5, 10, 15, and 20 A g^{-1} is shown in Fig. 7(f), whereas the fact is manifested that the C_{sp} value gradually reduces with increasing current density because of the diffusion and penetration of ions from the electrolyte to the supercapacitor electrode become interrupted at larger charging current.[77] Now the retention abilities of C_{sp} are found to be 67.09%, 72.49%, 80.30%, and 76.65% for pristine $Ti_3C_2T_x$, NS-CQD/M-5, NS-CQD/M-10, and NS-CQD/M-20, respectively as evaluated at a current density of 5 A g^{-1} when compared to the capacitance values at a current density of 1 A g^{-1}. At a higher current density of 20 A g^{-1}, the retention abilities are obtained as 50.45%, 53.14%, 59.38%, and 48.06% for pristine $Ti_3C_2T_x$, NS-CQD/M-5, NS-CQD/M-10, and NS-CQD/M-20, respectively, compared to their capacitance values at 1 A g^{-1}. Hence, it can be concluded that NS-CQD/M-10 possesses the maximum C_{sp} value and superior charge storage capability among the other as-synthesized samples. To realize a material as an efficient supercapacitor electrode for practical application in the domain of energy storage, cycling retention plays a momentous role. The cycling stabilities of the three $Ti_3C_2T_x$ hybrids have been accounted for 10 000 charging–discharging cycles at a higher current density of 10 A g^{-1} (as shown in Fig. 8(h)) within the voltage window varying from −0.65 V to +0.65 V in 1 M H_2SO_4 electrolyte. NS-CQD/M-5 and NS-CQD/M-20 retained 95.5% and 94.1% of their initial values, respectively, whereas NS-CQD/M-10 retained 98.3% of its initial value. Here, two coin cells prepared with NS-CQD/M-10 were connected in series to ignite a red LED (as shown in the inset of Fig. 8(h)). The videography, circuit diagram, and digital photograph are provided in the ESI (Fig. S9†). The energy and power density values of the best-performing sample, *i.e.*, NS-CQD/M-10, were obtained using eqn (3) & (4), and the energy density is found to be 170.34 W h kg^{-1} at a power density of 1290.98 W kg^{-1} and preserves up to 136.78 W h kg^{-1} at a greater power density of 6539.68 W kg^{-1}. Fig. 8(i) shows the Ragone plot of the NS-CQD/M-10 sample, indicating improved energy and power densities with the comparison of other Ti_3C_2 MXene- and CQD-based materials reported in the literature. In addition, Table 1 describes a comparative dataset of the electrochemical performances of formerly literature-reported supercapacitor electrodes with the as-obtained NS-CQD/M electrodes.

3.6. Electrochemical impedance spectroscopy (EIS) analysis

EIS is used as a fingerprint technique to investigate ion transfer, internal resistance, and kinetics of charge transport of the electrochemical systems further by investigating Nyquist plots. Fig. 9(a) demonstrates the typical Nyquist plots of pristine $Ti_3C_2T_x$ along with three other as-synthesized composite materials within a frequency range varying from 0.1 Hz to 100 kHz. Herein, Fig. 9(b) illustrates the high-frequency region of Nyquist plots for all the investigated samples including an equivalent circuit model and the accurate values of the parameters such as equivalent series resistance (R_s), charge trans-

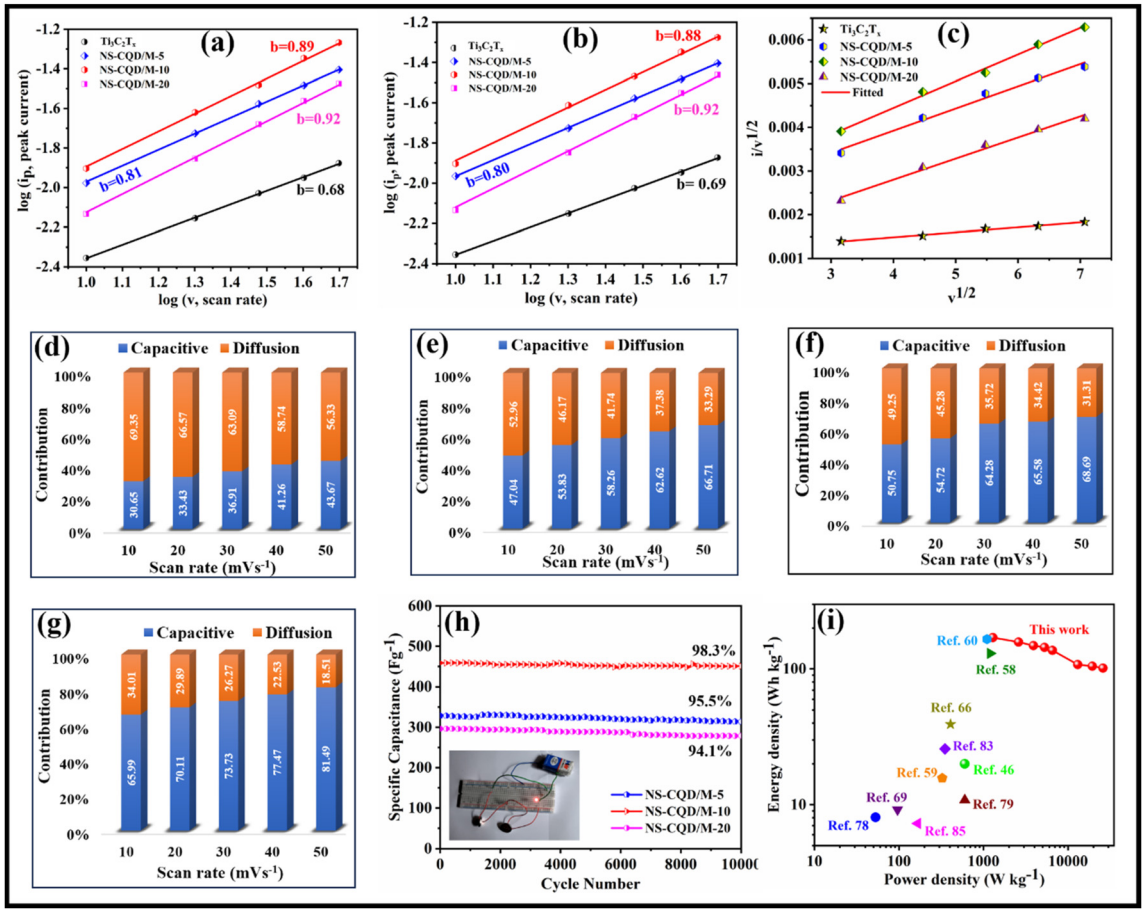

Fig. 8 Log (i_p, peak current) *vs.* log (v, scan rate) of the (a) anode, (b) cathode, and (c) $v^{1/2}$ *vs.* $i/v^{1/2}$ of all synthesized samples; contribution of the capacitive-controlled and diffusion-controlled capacitances of four samples: (d) pristine $Ti_3C_2T_x$, (e) NS-CQD/M-5, (f) NS-CQD/M-10, and (g) NS-CQD/M-20; (h) cycling stability of the NS-CQD/M-5, NS-CQD/M-10 and NS-CQD/M-20 composites at a current density of 10 A g^{-1} over 10 000 cycles (inset: digital photograph of a burning LED), and (i) Ragone plot of NS-CQD/M-10 in comparison with other literature reported CQD- and MXene-based composites.

fer resistance (R_{ct}), Warburg impedance (W_0), and the constant phase element (CPE) of the EIS system estimated from fitted high-frequency zone. In the present work, a modified Randles circuit is employed to obtain a proper fit over a wide frequency range, where CPE is utilised instead of a conventional capacitor. Here, the value of R_s, which implies the intrinsic resistance of the electrode, electrolyte solution, and the contact resistance between the active electrode material and the electrolyte solution at the interface,[86] was measured from the intersection value of the semi-circular EIS fitted plot on the real Z' axis. From the magnified portion of the high-frequency part (Fig. 9(b)), it is observed that all the studied sample electrodes exhibit comparatively lower R_s values, manifesting a desirable electrical conductivity. The fitted EIS curves of pristine $Ti_3C_2T_x$, NS-CQD/M-5, NS-CQD/M-10, and NS-CQD/M-20 are shown in Fig. 9(c), (d), (e), and (f), respectively. The R_{ct} value, which is estimated from the diameter of the semi-circle segment of the Nyquist plot in the intermediate frequency zone, corroborates the obstruction of electrolyte ion transfer between the electrolyte and the operative electrode material. Herein, the lowest R_{ct} value of NS-CQD/M-10 assures comparatively more spontaneous electrolyte ion transfer between the electrolyte and the electrode than the other three samples. Moreover, the parameter W_0 explains the mechanism of electrolyte ion diffusion. The fitted values of all extracted parameters for the studied samples are summarised in Table S3.† Analysing these parameters, it can be observed that the most efficient composite, *i.e.*, NS-CQD/M-10, shows the lowest R_s, R_{ct}, and W_0 values compared to the other as-prepared composites and pristine $Ti_3C_2T_x$, corroborating with the electrochemical performance, and it shows that the modification of the doping concentration of N and S within CQDs attached in the $Ti_3C_2T_x$ matrix ameliorates the ion diffusion rate and charge transfer from the electrolyte to the active electrode material.

Effectively, the introduction of NS-CQDs into the $Ti_3C_2T_x$ matrix serves as a spacer that expands the effective specific surface area, which is beneficial for electrochemical reactions. Additionally, N-, S-, and O-containing functional groups of NS-CQDs stimulate additional redox-active sites, leading to

Table 1 Comparison table of the supercapacitive performances of the present work with other literature reported electrodes

Materials	Electrolytes	Specific capacitance (at a scan rate or current density)	Cycling stability	Ref.
N-doped Ti_3C_2	1 M H_2SO_4	192 F g^{-1} at 1 mV s^{-1}	92%/10 000 cycles	78
N,O co-doped C@Ti_3C_2	6 M KOH	250.6 F g^{-1} at 1 A g^{-1}	94%/5000 cycles	79
Ti_3C_2/rGO	1 M H_2SO_4	233 F g^{-1} at 1 A g^{-1}	91.1%/10 000 cycles	80
MoS_2/Ti_3C_2	1 M H_2SO_4	342 F g^{-1} at 0.4 A g^{-1}	99%/10 000 cycles	81
EDA–Ti_3C_2	1 M H_2SO_4	486.2 F g^{-1} at 2 mV s^{-1}	89.7%/10 000 cycles	82
CQD/Ti_3C_2	1 M H_2SO_4	441 F g^{-1} at 1 A g^{-1}	96.2%/10 000 cycles	83
Carbon nanofibre/GQDs	6 M KOH	200 F g^{-1} at 1 A g^{-1}	98%/10 000 cycles	84
Strontium cobaltite/N-doped CQDs	0.5 M $NaPF_6$	180.24 F g^{-1} at 0.5 A g^{-1}	80.8%/5000 cycles	85
Porous Ti_3CN/CDs	1 M H_2SO_4	688.9 F g^{-1} at 2 A g^{-1}	90%/10 000 cycles	46
Ti_3C_2/calcium alginate-derived CDs	3 M H_2SO_4	372.6 F g^{-1} at 1 A g^{-1}	93.5%/30 000 cycles	47
N,S CQDs/Ti_3C_2	1 M H_2SO_4	725.7 F g^{-1} at 1 A g^{-1}	98.3%/10 000 cycles	This work

EDA – ethylenediamine, CDs – carbon dots, and GQDs – graphene quantum dots.

reduced electrolyte ion transfer resistance and improved electrode kinetics as well. Thus, the synergistic effect of the modification of N and S co-doping within the CQD network and the growth of NS-CQDs within $Ti_3C_2T_x$ sheets encourages for enhanced electrochemical performance and superior cycling stability. It can be proclaimed that this hybrid electrode with excellent electrochemical properties can enlighten in the field of energy storage applications.

3.7. BET data analysis

Structural factors, particularly specific surface area and porosity, significantly influence electrochemical performance and kinetics. To investigate these characteristics, N_2 adsorption–desorption isotherms of pristine $Ti_3C_2T_x$ and the best-performing composite, NS-CQD/M-10, were obtained at 77.35 K and are presented in Fig. 10(a). Using BET theory, the specific surface area values were computed, corroborating that the NS-CQD/M-10 hybrid exhibits a significantly greater specific surface area (70.51 m^2 g^{-1}) compared to that of bare $Ti_3C_2T_x$ (23.58 m^2 g^{-1}). It is evident that NS-CQDs inserted between $Ti_3C_2T_x$ layers prevent restacking and enlarge the interlayer spacing of the 2D $Ti_3C_2T_x$ sheets, thereby enhancing the specific surface area. Moreover, Fig. 10(b) shows the BJH pore size distribution curves of pristine $Ti_3C_2T_x$ and the NS-CQD/M-10 composite. The pore width and pore volume were obtained using non-local density functional theory (NLDFT). The pore size distribution curves reveal that the NS-CQD/M-10 composite possesses a larger pore volume (0.181 cc g^{-1}) than that of pristine $Ti_3C_2T_x$ (0.010 cc g^{-1}). Consequently, the composite, with its improved active surface area and porous structure compared to bare $Ti_3C_2T_x$, is more compatible for efficient ion transport and enhanced electrochemical performance.

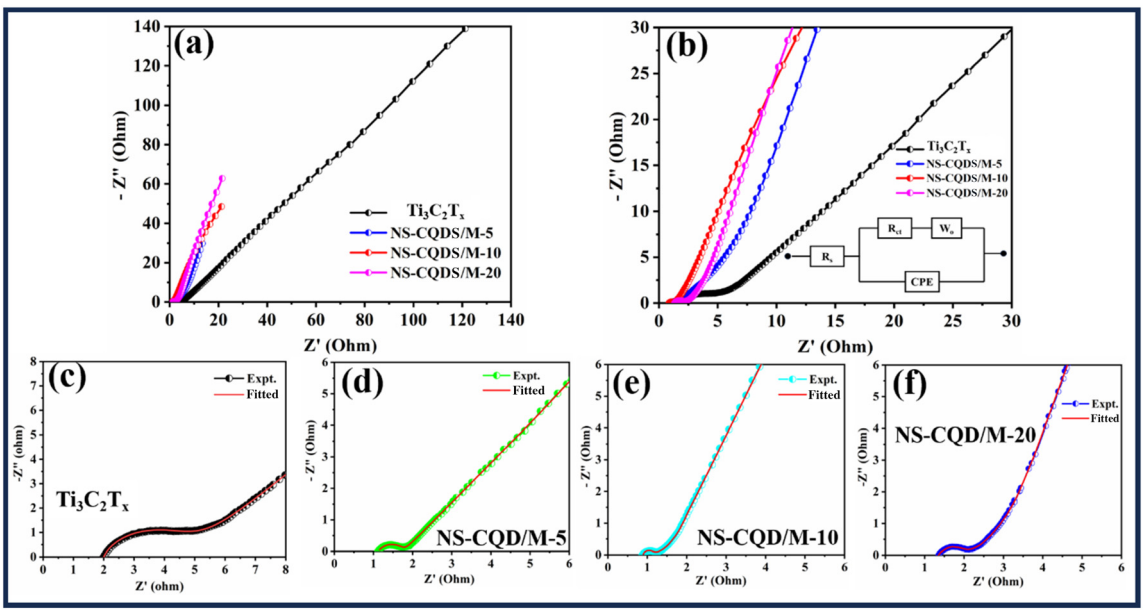

Fig. 9 (a) Nyquist plots of pristine $Ti_3C_2T_x$ along with the three composites, (b) high-frequency portion of Nyquist plots, and the fitted high-frequency part of Nyquist plots of (c) pristine $Ti_3C_2T_x$, (d) NS-CQD/M-5, (e) NS-CQD/M-10, and (f) NS-CQD/M-20.

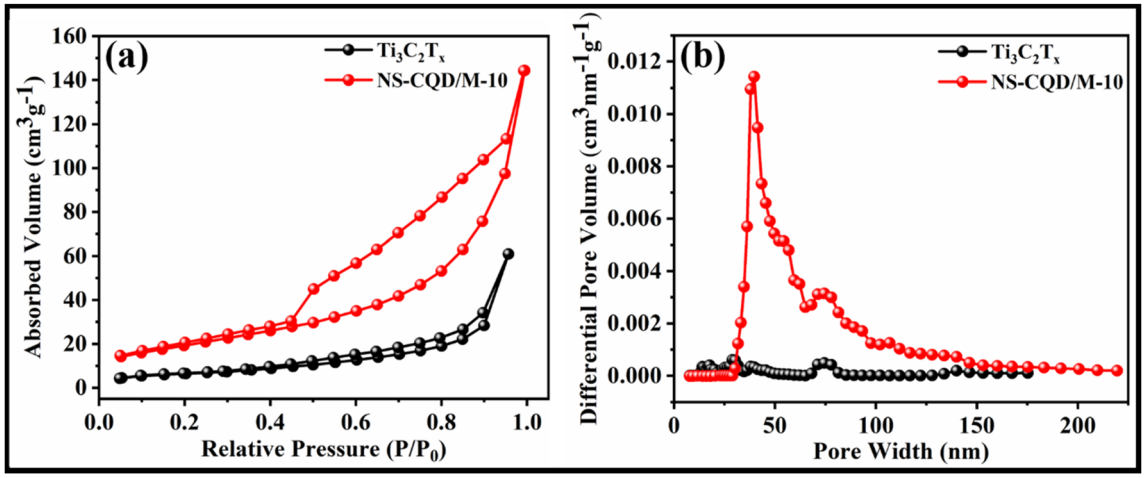

Fig. 10 (a) N_2 adsorption–desorption isotherms and (b) BJH pore size distribution curves of pristine $Ti_3C_2T_x$ and NS-CQD/M-10.

4. Conclusions

In summary, NS-CQDs have been successfully introduced within $Ti_3C_2T_x$ MXene stacked layers *via* a facile hydrothermal approach for constructing NS-CQD/M hybrids. NS-CQDs as conductive spacers are not only indisputably effective in staving off the unavoidable restacking issue of $Ti_3C_2T_x$ but also expand interlayer spacing, resulting in an enlargement of the specific surface area of $Ti_3C_2T_x$ and the activation of excessive surface functional groups stimulating faradaic behaviour. Benefitting from the synergistic effect of co-doping modification of N and S (acting as trap states), upon introduction of CQDs and the 2D $Ti_3C_2T_x$ matrix with high electrical conductivity and superior electrochemical activity, this unique 0D/2D heterostructure composite NS-CQD/M-10 delivers a remarkably superior C_{sp} value of 725.7 F g^{-1} at a current density of 1 A g^{-1} within a voltage window of −0.65 to +0.65 V compared to those of pristine $Ti_3C_2T_x$ and other NS-CQD/M hybrids. Based on the NS-CQD/M electrode, the assembled symmetrical supercapacitor device exhibits a remarkable capacitance retention of 80.30% at a current density of 5 A g^{-1} and 59.38% at a higher current density of 20 A g^{-1}, respectively, relative to the value of 1 A g^{-1} and a tremendous cycling stability of 98.3% over 10 000 cycles at 10 A g^{-1}. Moreover, this as-synthesized hybrid NS-CQD/M-10 exhibits an outstanding energy density of 170.34 W h kg^{-1} at a power density of 1290.98 W kg^{-1}. Hence, perceiving the noteworthy attributes and the extraordinary electrochemical activity of the NS-CQD/M synergistic hybrid, it can be corroborated that this 0D/2D heterostructure-based composite can be a promising high-performance electrode material that extends the avenue of supercapacitors in the forthcoming energy storage and commercial applications.

Author contributions

Srija Ghosh: writing – review & editing, writing – original draft, methodology, investigation, data curation, formal analysis, visualization, and conceptualization. Sumanta Bera: writing – review & editing, writing – original draft, investigation, formal analysis, data curation, and conceptualization. Arijit Kapuria: validation, investigation, formal analysis, and data curation. Anup Debnath: software, writing – review & editing, investigation, and formal analysis. Pratyusha Das: writing – review & editing, validation, formal analysis, data curation, and conceptualization. Yan-Kuin Su: validation, formal analysis, and data curation. Shyamal K. Saha: writing – review & editing, writing – original draft, supervision, resources, methodology, investigation, data curation, visualization, and conceptualization.

Data availability

The data that support the findings of this study are available from the corresponding author upon reasonable request.

Conflicts of interest

The authors declare that there are no conflicts of interest.

Acknowledgements

SG acknowledges the Indian Association for the Cultivation of Science (IACS) for providing a fellowship. SB acknowledges University Grants Commission (UGC) for awarding a fellowship. AK and PD acknowledge the Council of Scientific Industrial Research (CSIR). AD acknowledges Pachhunga University College (PUC), India for providing infrastructural facilities. Yan-Kuin Su acknowledges AISSM, NCKU. SKS acknowledges IACS and AISSM, NCKU for providing infrastructural and financial support.

References

1 S. Chu and A. Majumdar, Opportunities and challenges for a sustainable energy future, *Nature*, 2012, **488**, 294–303.
2 T. M. Gür, Review of electrical energy storage technologies, materials and systems: challenges and prospects for large-scale grid storage, *Energy Environ. Sci.*, 2018, **11**, 2696–2767.
3 H. D. Yoo, E. Markevich, G. Salitra, D. Sharon and D. Aurbach, On the challenge of developing advanced technologies for electrochemical energy storage and conversion, *Mater. Today*, 2014, **17**, 110–121.
4 S. Fleischmann, J. B. Mitchell, R. Wang, C. Zhan, D. Jiang, V. Presser and V. Augustyn, Pseudocapacitance: from fundamental understanding to high power energy storage materials, *Chem. Rev.*, 2020, **120**, 6738–6782.
5 J. Zhou, J. Yu, L. Shi, Z. Wang, H. Liu, B. Yang, C. Li, C. Zhu and J. Xu, A conductive and highly deformable all–pseudocapacitive composite paper as supercapacitor electrode with improved areal and volumetric capacitance, *Small*, 2018, **14**, 1803786.
6 Y. Yoon, M. Lee, S. K. Kim, G. Bae, W. Song, S. Myung, J. Lim, S. S. Lee, T. Zyung and K. An, A strategy for synthesis of carbon nitride induced chemically doped 2D MXene for high–performance supercapacitor electrodes, *Adv. Energy Mater.*, 2018, **8**, 1703173.
7 J. Zhao, H. Li, C. Li, Q. Zhang, J. Sun, X. Wang and J. Guo, MOF for template-directed growth of well-oriented nanowire hybrid arrays on carbon nanotube fibers for wearable electronics integrated with triboelectric nanogenerators, *Nano Energy*, 2018, **45**, 420–431.
8 J. Jang, J. Bae, M. Choi and S. Yoon, Fabrication and characterization of polyaniline coated carbon nanofiber for supercapacitor, *Carbon*, 2005, **43**, 2730–2736.
9 C. Zhang, W. Lv, Y. Tao and Q. Yang, Towards superior volumetric performance: design and preparation of novel carbon materials for energy storage, *Energy Environ. Sci.*, 2015, **8**, 1390–1403.
10 G. A. Snook, P. Kao and A. S. Best, Conducting-polymer-based supercapacitor devices and electrodes, *J. Power Sources*, 2011, **196**, 1–12.
11 Y. Ma, X. Xie, W. Yang, Z. Yu, X. Sun, Y. Zhang and X. Yang, Recent advances in transition metal oxides with different dimensions as electrodes for high-performance supercapacitors, *Adv. Compos. Hybrid Mater.*, 2021, 1–19.
12 Y. Huang, J. Liang and Y. Chen, An overview of the applications of graphene–based materials in supercapacitors, *Small*, 2012, **8**, 1805–1834.
13 J. H. Lee, N. Park, B. G. Kim, D. S. Jung, K. Im, J. Hur and J. W. Choi, Restacking-inhibited 3D reduced graphene oxide for high performance supercapacitor electrodes, *ACS Nano*, 2013, **7**, 9366–9374.
14 H. Kim, S. Bak, S. W. Lee, M. Kim, B. Park, S. C. Lee and Y. J. Choi, Scalable fabrication of micron-scale graphene nanomeshes for high-performance supercapacitor applications, *Energy Environ. Sci.*, 2016, **9**, 1270–1281.
15 L. Lin, W. Lei, S. Zhang, Y. Liu, G. G. Wallace and J. Chen, Two-dimensional transition metal dichalcogenides in supercapacitors and secondary batteries, *Energy Storage Mater.*, 2019, **19**, 408–423.
16 Q. Meng, K. Cai, Y. Chen and L. Chen, Research progress on conducting polymer based supercapacitor electrode materials, *Nano Energy*, 2017, **36**, 268–285.
17 F. Ahmad, A. Shahzad, M. Danish, M. Fatima, M. Adnan, S. Atiq, M. Asim, M. A. Khan, Q. U. Ain and R. Perveen, Recent developments in transition metal oxide-based electrode composites for supercapacitor applications, *J. Energy Storage*, 2024, **81**, 110430.
18 D. Sheberla, J. C. Bachman, J. S. Elias, C. Sun, Y. Shao-Horn and M. Dincă, Conductive MOF electrodes for stable supercapacitors with high areal capacitance, *Nat. Mater.*, 2017, **16**, 220–224.
19 B. Anasori, M. R. Lukatskaya and Y. Gogotsi, 2D metal carbides and nitrides (MXenes) for energy storage, *Nat. Rev. Mater.*, 2017, **2**, 1–17.
20 M. Hu, H. Zhang, T. Hu, B. Fan, X. Wang and Z. Li, Emerging 2D MXenes for supercapacitors: status, challenges and prospects, *Chem. Soc. Rev.*, 2020, **49**, 6666–6693.
21 Y. Liu, P. Zhang, N. Sun, B. Anasori, Q. Zhu, H. Liu, Y. Gogotsi and B. Xu, Self–assembly of transition metal oxide nanostructures on MXene nanosheets for fast and stable lithium storage, *Adv. Mater.*, 2018, **30**, 1707334.
22 M. Naguib, M. Kurtoglu, V. Presser, J. Lu, J. Niu, M. Heon, L. Hultman, and Y. Gogotsi and M. W. Barsoum, Two-dimensional nanocrystals produced by exfoliation of Ti_3AlC_2, in *MXenes*, Jenny Stanford Publishing, 2011, pp. 15–29.
23 M. R. Lukatskaya, S. M. Bak, X. Yu, X. Q. Yang, M. W. Barsoum and Y. Gogotsi, Probing the mechanism of high capacitance in 2D titanium carbide using in situ X-ray absorption spectroscopy, *Adv. Energy Mater.*, 2015, **5**, 2–5.
24 R. Ma, Z. Chen, D. Zhao, X. Zhang, J. Zhuo, Y. Yin, X. Wang, G. Yang and F. Yi, $Ti_3C_2T_x$ MXene for electrode materials of supercapacitors, *J. Mater. Chem. A*, 2021, **9**, 11501–11529.
25 H. Shao, K. Xu, Y. Wu, A. Iadecola, L. Liu, H. Ma and L. Qu, Unraveling the charge storage mechanism of $Ti_3C_2T_x$ MXene electrode in acidic electrolyte, *ACS Energy Lett.*, 2020, **5**, 2873–2880.
26 X. Zhao, C. Dall'Agnese, X. Chu, S. Zhao, G. Chen, Y. Gogotsi, Y. u Gao and Y. Dall'Agnese, Electrochemical behavior of $Ti_3C_2T_x$ MXene in environmentally friendly methanesulfonic acid electrolyte, *ChemSusChem*, 2019, **12**, 4480–4486.
27 M. Balogun, W. Qiu, W. Wang, P. Fang, X. Lu and Y. Tong, Recent advances in metal nitrides as high-performance electrode materials for energy storage devices, *J. Mater. Chem. A*, 2015, **3**, 1364–1387.
28 H. Xu, D. Zheng, F. Liu, W. Li and J. Lin, Synthesis of an MXene/polyaniline composite with excellent electrochemical properties, *J. Mater. Chem. A*, 2020, **8**, 5853–5858.

29 M. Boota, B. Anasori, C. Voigt, M. Zhao, M. W. Barsoum and Y. Gogotsi, Pseudocapacitive electrodes produced by oxidant-free polymerization of pyrrole between the layers of 2D titanium carbide (MXene), *Adv. Mater.*, 2016, **28**, 1517–1522.

30 M. Mahmood, A. Rasheed, I. Ayman, T. Rasheed, S. Munir, S. Ajmal, P. O. Agboola, M. F. Warsi and M. Shahid, Synthesis of ultrathin MnO_2 nanowire-intercalated 2D-MXenes for high-performance hybrid supercapacitors, *Energy Fuels*, 2021, **35**, 3469–3478.

31 W. Luo, Y. Sun, Z. Lin, X. Li, Y. Han, J. Ding, T. Li, C. Hou and Y. Ma, Flexible $Ti_3C_2T_x$ MXene/V_2O_5 composite films for high-performance all-solid supercapacitors, *J. Energy Storage*, 2023, **62**, 106807.

32 K. Nasrin, V. Sudharshan, K. Subramani and M. Sathish, Insights into 2D/2D MXene heterostructures for improved synergy in structure toward next–generation supercapacitors: a review, *Adv. Funct. Mater.*, 2022, **32**, 2110267.

33 W. Luo, Q. Liu, B. Zhang, J. Li, R. Li, T. Li, Z. Sun and Y. Ma, Binder-free flexible $Ti_3C_2T_x$ MXene/reduced graphene oxide/carbon nanotubes film as electrode for asymmetric supercapacitor, *Chem. Eng. J.*, 2023, **474**, 145553.

34 Y. Wang and A. Hu, Carbon quantum dots: synthesis, properties and applications, *J. Mater. Chem. C*, 2014, **2**, 6921–6939.

35 S. Yang, J. Sun, X. Li, W. Zhou, Z. Wang, P. He, G. Ding, X. Xie, Z. Kang and M. Jiang, Large-scale fabrication of heavy doped carbon quantum dots with tunable-photoluminescence and sensitive fluorescence detection, *J. Mater. Chem. A*, 2014, **2**, 8660–8667.

36 F. Yuan, S. Li, Z. Fan, X. Meng, L. Fan and S. Yang, Shining carbon dots: Synthesis and biomedical and optoelectronic applications, *Nano Today*, 2016, **11**, 565–586.

37 K. Dave and V. G. Gomes, Carbon quantum dot-based composites for energy storage and electrocatalysis: Mechanism, applications and future prospects, *Nano Energy*, 2019, **66**, 104093.

38 F. Yuan, S. Li, Z. Fan, X. Meng, L. Fan and S. Yang, Shining carbon dots: Synthesis and biomedical and optoelectronic applications, *Nano Today*, 2016, **11**, 565–586.

39 A. Dager, T. Uchida, T. Maekawa and M. Tachibana, Synthesis and characterization of mono-disperse carbon quantum dots from fennel seeds: photoluminescence analysis using machine learning, *Sci. Rep.*, 2019, **9**, 14004.

40 K. Qu, M. Chen, W. Wang, S. Yang, S. Jing, S. Guo, J. Tian, H. Qi and Z. Huang, Biomass-derived carbon dots regulating nickel cobalt layered double hydroxide from 2D nanosheets to 3D flower-like spheres as electrodes for enhanced asymmetric supercapacitors, *J. Colloid Interface Sci.*, 2022, **616**, 584–594.

41 H. Lv, X. Gao, Q. Xu, H. Liu, Y. Wang and Y. Xia, Carbon quantum dot-induced MnO_2 nanowire formation and construction of a binder-free flexible membrane with excellent superhydrophilicity and enhanced supercapacitor performance, *ACS Appl. Mater. Interfaces*, 2017, **9**, 40394–40403.

42 Y. Zhu, X. Ji, C. Pan, Q. Sun, W. Song, L. Fang, Q. Chen and C. E. Banks, A carbon quantum dot decorated RuO_2 network: outstanding supercapacitances under ultrafast charge and discharge, *Energy Environ. Sci.*, 2013, **6**, 3665–3675.

43 X. Jian, H. Yang, J. Li, E. Zhang and Z. Liang, Flexible all-solid-state high-performance supercapacitor based on electrochemically synthesized carbon quantum dots/polypyrrole composite electrode, *Electrochim. Acta*, 2017, **228**, 483–493.

44 Z. Zhao and Y. Xie, Enhanced electrochemical performance of carbon quantum dots-polyaniline hybrid, *J. Power Sources*, 2017, **337**, 54–64.

45 Z. Tan, W. Wang, M. Zhu, Y. Liu, Y. Yang, X. Ji and Z. He, Ti3C2Tx MXene@ carbon dots hybrid microflowers as a binder-free electrode material toward high capacity capacitive deionization, *Desalination*, 2023, **548**, 116267.

46 Y. Wang, N. Chen, B. Zhou, X. Zhou, B. Pu, J. Bai, Q. Tang, Y. Liu and W. Yang, NH_3-induced in situ etching strategy derived 3D-interconnected porous MXene/carbon dots films for high performance flexible supercapacitors, *Nanomicro Lett.*, 2023, **15**, 231.

47 P. Zhang, J. Li, D. Yang, R. A. Soomro and B. Xu, Flexible carbon dots–intercalated MXene film electrode with outstanding volumetric performance for supercapacitors, *Adv. Funct. Mater.*, 2023, **33**, 2209918.

48 S. Gu, C. Hsieh, Y. Tsai, Y. A. Gandomi, S. Yeom, K. D. Kihm, C. Fu and R. Juang, Sulfur and nitrogen co-doped graphene quantum dots as a fluorescent quenching probe for highly sensitive detection toward mercury ions, *ACS Appl. Nano Mater.*, 2019, **2**, 790–798.

49 H. Chen, F. Yu, G. Wang, L. Chen, B. Dai and S. Peng, Nitrogen and sulfur self-doped activated carbon directly derived from elm flower for high-performance supercapacitors, *ACS Omega*, 2018, **3**, 4724–4732.

50 J. Yan, Q. Wang, T. Wei and Z. Fan, Recent advances in design and fabrication of electrochemical supercapacitors with high energy densities, *Adv. Energy Mater.*, 2014, **4**, 1300816.

51 M. Miah, S. Bhattacharya, A. Gupta and S. K. Saha, Origin of high storage capacity in N-doped graphene quantum dots, *Electrochim. Acta*, 2016, **222**, 709–716.

52 Z. Ouyang, Y. Lei, Y. Chen, Z. Zhang, Z. Jiang, J. Hu and Y. Lin, Preparation and specific capacitance properties of sulfur, nitrogen co-doped graphene quantum dots, *Nanoscale Res. Lett.*, 2019, **14**, 1–9.

53 M. Alhabeb, K. Maleski, B. Anasori, P. Lelyukh, L. Clark, S. Sin and Y. Gogotsi, Guidelines for synthesis and processing of two-dimensional titanium carbide ($Ti_3C_2T_x$ MXene), *Chem. Mater.*, 2017, **29**, 7633–7644.

54 H. M. Rietveld, A profile refinement method for nuclear and magnetic structures, *J. Appl. Crystallogr.*, 1969, **2**, 65–71.

55 L. Lutterotti, S. Matthies and H. Wenk, MAUD: a friendly Java program for material analysis using diffraction, *CPD Newsletter*, 1999, **21**, 14–15.

56 P. Hota, M. Miah, S. Bose, D. Dinda, U. K. Ghorai, Y. Su and S. K. Saha, Ultra-small amorphous MoS_2 decorated

reduced graphene oxide for supercapacitor application, *J. Mater. Sci. Technol.*, 2020, **40**, 196–203.

57 S. Maity, S. Bera, A. Kapuria, A. Debnath, S. Das and S. K. Saha, MXene derived metal organic framework@PANI heterostructure as a hybrid supercapacitor, *Mater. Today Chem.*, 2025, **45**, 102690.

58 P. Das, T. K. Mondal, S. Bera, S. Das, H. Hsu, Y. Su and S. K. Saha, Facile *in situ* growth of spore-like silica on layered MXene sheets for potential application in Supercapacitor, *Electrochim. Acta*, 2023, **465**, 142983.

59 J. Li, X. Yun, Z. Hu, L. Xi, N. Li, H. Tang, P. Lu and Y. Zhu, Three-dimensional nitrogen and phosphorus co-doped carbon quantum dots/reduced graphene oxide composite aerogels with a hierarchical porous structure as superior electrode materials for supercapacitors, *J. Mater. Chem. A*, 2019, **7**, 26311–26325.

60 S. Bera, T. K. Mondal, Y. Su and S. K. Saha, Sulfur-tuned MoS_2 quantum dot decorated $Ti_3C_2T_x$ (MXene) electrode materials for high performance supercapacitor applications, *J. Alloys Compd.*, 2024, **985**, 174010.

61 Z. Jiao-qun, M. Bing-chu and C. Yan-lin, Preparation of Ti_3SiC_2 with aluminum by means of spark plasma sintering, *J. Wuhan Univ. Technol., Mater. Sci. Ed.*, 2003, **18**, 37–40.

62 T. Rasheed, A. Rasheed, S. Munir, S. Ajmal, Z. M. Shahzad, I. A. Alsafari, S. A. Ragab, P. O. Agboola and I. Shakir, A cost-effective approach to synthesize $NiFe_2O_4$/MXene heterostructures for enhanced photodegradation performance and anti-bacterial activity, *Adv. Powder Technol.*, 2021, **32**, 2248–2257.

63 R. Sun, H. Zhang, J. Liu, X. Xie, R. Yang, Y. Li, S. Hong and Z. Yu, Highly conductive transition metal carbide/carbonitride (MXene)@polystyrene nanocomposites fabricated by electrostatic assembly for highly efficient electromagnetic interference shielding, *Adv. Funct. Mater.*, 2017, **27**, 1702807.

64 L. Xiu, Z. Wang, M. Yu, X. Wu and J. Qiu, Aggregation-resistant 3D MXene-based architecture as efficient bifunctional electrocatalyst for overall water splitting, *ACS Nano*, 2018, **12**, 8017–8028.

65 J. Shen, S. Shang, X. Chen, D. Wang and Y. Cai, Highly fluorescent N, S-co-doped carbon dots and their potential applications as antioxidants and sensitive probes for Cr(VI) detection, *Sens. Actuators, B*, 2017, **248**, 92–100.

66 A. Kapuria, T. K. Mondal, B. K. Shaw, Y. Su and S. K. Saha, Polysulfide functionalized reduced graphene oxide for electrocatalytic hydrogen evolution reaction and supercapacitor applications, *Int. J. Hydrogen Energy*, 2023, **48**, 17014–17025.

67 Y. Sang, Z. Zhao, M. Zhao, P. Hao, Y. Leng and H. Liu, From UV to near-infrared, WS_2 nanosheet: a novel photocatalyst for full solar light spectrum photodegradation, *Adv. Mater.*, 2014, **27**, 363–369.

68 A. Debnath, S. Bhattacharya and S. K. Saha, Transition from antiferromagnetic to ferromagnetic β-$Co(OH)_2$ with higher Curie temperature, *J. Phys. D:Appl. Phys.*, 2020, **53**, 225004.

69 P. Zhang, Q. Zhu, R. A. Soomro, S. He, N. Sun, N. Qiao and B. Xu, In situ ice template approach to fabricate 3D flexible MXene film–based electrode for high performance supercapacitors, *Adv. Funct. Mater.*, 2020, **30**, 2000922.

70 Y. Cao, Q. Deng, Z. Liu, D. Shen, T. Wang, Q. Huang, S. Du, N. Jiang, C. Lin and J. Yu, Enhanced thermal properties of poly (vinylidene fluoride) composites with ultrathin nanosheets of MXene, *RSC Adv.*, 2017, **7**, 20494–20501.

71 W. Y. Chen, X. Jiang, S. Lai, D. Peroulis and L. Stanciu, Nanohybrids of a MXene and transition metal dichalcogenide for selective detection of volatile organic compounds, *Nat. Commun.*, 2020, **11**, 1302.

72 Y. Xu, D. Li, M. Liu, F. Niu, J. Liu and E. Wang, Enhanced-quantum yield sulfur/nitrogen co-doped fluorescent carbon nanodots produced from biomass Enteromorpha prolifera: synthesis, posttreatment, applications and mechanism study, *Sci. Rep.*, 2017, **7**, 4499.

73 G. S. Lee, T. Yun, H. Kim, I. H. Kim, J. Choi, S. H. Lee and H. J. Lee, Mussel inspired highly aligned $Ti_3C_2T_x$ MXene film with synergistic enhancement of mechanical strength and ambient stability, *ACS Nano*, 2020, **14**, 11722–11732.

74 M. R. Pallavolu, N. Gaddam, A. N. Banerjee, R. R. Nallapureddy and S. W. Joo, Superior energy–power performance of N–doped carbon nano–onions–based asymmetric and symmetric supercapacitor devices, *Int. J. Energy Res.*, 2022, **46**, 1234–1249.

75 M. C. Daugherty, S. Gu, D. S. Aaron, B. C. Mallick, Y. A. Gandomi and C. Hsieh, Decorating sulfur and nitrogen co-doped graphene quantum dots on graphite felt as high-performance electrodes for vanadium redox flow batteries, *J. Power Sources*, 2020, **477**, 228709.

76 Z. Li, X. Liu, L. Wang, F. Bu, J. Wei, D. Pan and M. Wu, Hierarchical 3D all–carbon composite structure modified with N–doped graphene quantum dots for high–performance flexible supercapacitors, *Small*, 2018, **14**, 1801498.

77 C. Yu, Y. Gong, R. Chen, M. Zhang, J. Zhou, J. An, F. Lv, S. Guo and G. Sun, A solid–state fibriform supercapacitor boosted by host–guest hybridization between the carbon nanotube scaffold and MXene nanosheets, *Small*, 2018, **14**, 1801203.

78 Y. Wen, T. E. Rufford, X. Chen, N. Li, M. Lyu, L. Dai and L. Wang, Nitrogen-doped $Ti_3C_2T_x$ MXene electrodes for high-performance supercapacitors, *Nano Energy*, 2017, **38**, 368–376.

79 Z. Pan and X. Ji, Facile synthesis of nitrogen and oxygen co-doped C@Ti_3C_2 MXene for high performance symmetric supercapacitors, *J. Power Sources*, 2019, **439**, 227068.

80 L. Shao, J. Xu, J. Ma, B. Zhai, Y. Li, R. Xu, Z. Ma, G. Zhang, C. Wang and J. Qiu, MXene/rGO composite aerogels with light and high-strength for supercapacitor electrode materials, *Compos. Commun.*, 2020, **19**, 108–113.

81 M. Chandran, A. Thomas, A. Raveendran, M. Vinoba and M. Bhagiyalakshmi, MoS_2 confined MXene heterostructures as electrode material for energy storage application, *J. Energy Storage*, 2020, **30**, 101446.

82 P. Xu, H. Xiao, X. Liang, T. Zhang, F. Zhang, C. Liu, B. Lang and Q. Gao, A MXene-based EDA-$Ti_3C_2T_x$ intercalation compound with expanded interlayer spacing as high performance supercapacitor electrode material, *Carbon*, 2021, **173**, 135–144.
83 Y. Wang, Y. Cui, D. Kong, X. Wang, B. Li, T. Cai and X. Li, Stimulation of surface terminating group by carbon quantum dots for improving pseudocapacitance of $Ti_3C_2T_x$ MXene based electrode, *Carbon*, 2021, **180**, 118–126.
84 J. Zhu, L. Wang, X. Gan, T. Tang, F. Qin, W. Luo and Q. Li, Graphene quantum dot inlaid carbon nanofibers: Revealing the edge activity for ultrahigh rate pseudocapacitive energy storage, *Energy Storage Mater.*, 2022, **47**, 158–166.
85 R. Kumari, P. R. Kharangarh, V. Singh, R. Jha and C. R. Kant, Sequential processing of nitrogen-rich, biowaste-derived carbon quantum dots combined with strontium cobaltite for enhanced supercapacitive performance, *J. Alloys Compd.*, 2023, **969**, 172256.
86 S. Bera, M. Miah, T. K. Mondal, A. Debnath and S. K. Saha, Synthesis of new mixed metal oxide $RuNi_2O_4$ phase decorated on reduced graphene oxide for supercapacitor applications, *Electrochim. Acta*, 2022, **424**, 140666.